# Mineralogy of Vera Rubin Ridge from the Mars Science Laboratory CheMin Instrument

E. B. Rampe[1*], T. F. Bristow[2], R. V. Morris[1], S. M. Morrison[3], C. N. Achilles[4], D. W. Ming[1], D. T. Vaniman[5], D. F. Blake[2], V. M. Tu[6], S. J. Chipera[5], A. S. Yen[7], T. S. Peretyazhko[6], R. T. Downs[8], R. M. Hazen[3], A. H. Treiman[9], J. P. Grotzinger[10], N. Castle[5], P. I. Craig[5], D. J. Des Marais[2], M. T. Thorpe[1], R. C. Walroth[2], G. W. Downs[8], A. A. Fraeman[7], K. L. Siebach[11], R. Gellert[12], B. Lafuente[13], A. C. McAdam[4], P.-Y. Meslin[14], B. Sutter[6], M. R. Salvatore[15]

[1]NASA Johnson Space Center, Houston, TX USA
[2]NASA Ames Research Center, Moffett Field, CA USA
[3]Carnegie Institute for Science, Washington, D.C. USA
[4]NASA Goddard Space Flight Center, Greenbelt, MD USA
[5]Planetary Science Institute, Tucson, AZ USA
[6]Jacobs at NASA Johnson Space Center, Houston, TX USA
[7]Jet Propulsion Laboratory, Pasadena, CA USA
[8]University of Arizona, Tucson, AZ USA
[9]Lunar and Planetary Institute, Houston, TX USA
[10]California Institute of Technology, Pasadena, CA USA
[11]Rice University, Houston, TX USA
[12]University of Guelph, Guelph, ON Canada
[13]SETI Institute, Mountain View, CA USA
[14]Université de Toulouse, CNS, UPS, CNES, Toulouse, France
[15]Northern Arizona University, Flagstaff, AZ USA
[*]corresponding author: elizabeth.b.rampe@nasa.gov

## Key Points

- Data from the CheMin X-ray diffractometer demonstrate a variety of secondary alteration products on Vera Rubin ridge.
- Hematite particle size changes across and below the ridge, and this change may be a marker of diagenetic reactions.
- The aqueous history of Vera Rubin ridge was complex, with several fluid episodes that varied in temperature, salinity, and pH.

## Abstract

Vera Rubin ridge (VRR) is an erosion-resistant feature on the northwestern slope of Mount Sharp in Gale crater, Mars, and orbital visible/short-wave infrared measurements indicate it contains red-colored hematite. The Mars Science Laboratory *Curiosity* rover performed an extensive campaign on VRR to study its mineralogy, geochemistry, and sedimentology to determine the depositional and diagenetic history of the ridge and constrain the processes by which the hematite could have formed. X-ray diffraction (XRD) data from the CheMin instrument of four samples drilled on and below VRR demonstrate differences in iron,

phyllosilicate, and sulfate mineralogy and hematite grain size. Hematite is common across the ridge, and its detection in a gray-colored outcrop suggested localized regions with coarse-grained hematite, which commonly forms from warm fluids. Broad XRD peaks for hematite in one sample below VRR and the abundance of $FeO_T$ in the amorphous component suggest the presence of nano-crystalline hematite and amorphous Fe oxides/oxyhydroxides. Well-crystalline akaganeite and jarosite are present in two samples drilled from VRR, indicating at least limited alteration by acid-saline fluids. Collapsed nontronite is present below VRR, but samples from VRR contain phyllosilicate with d(001) = 9.6 Å, possibly from ferripyrophyllite or an acid-altered smectite. The most likely cementing agents creating the ridge are hematite and opaline silica. We hypothesize late diagenesis can explain much of the mineralogical variation on the ridge, where multiple fluid episodes with variable pH, salinity, and temperature altered the rocks, causing the precipitation and crystallization of phases that are not otherwise in equilibrium.

**Plain language summary**

Vera Rubin ridge (VRR) is an erosion-resistant feature on the northwestern slope of Mount Sharp in Gale crater, Mars, and it contains the Fe(III) oxide mineral hematite. Hematite is an especially important mineral to study on the martian surface because it commonly forms in the presence of liquid water. Identifying the processes that formed hematite on VRR can help constrain the history of liquid water in Gale crater. The Mars Science Laboratory *Curiosity* rover performed an extensive campaign on VRR to determine the geologic history of the ridge. Mineralogical data collected by the CheMin instrument of four rock samples drilled on and below the ridge demonstrate changes in the mineralogy and provide clues about the aqueous history of VRR. Red hematite is common across the ridge, but detection of gray hematite in one sample indicates the presence of localized coarse-grained hematite, which commonly forms under warm temperatures. Minerals that form in acidic, saline solutions were found in two samples, indicating localized alteration in acidic and relatively salty waters. We hypothesize that multiple episodes of groundwater with variable pH, salinity, and temperature altered the sediments after they lithified.

**Index terms and keywords**

5470 Surface materials and properties

5410 Composition (1060, 3672)

3617 Alteration and weathering processes (1039)

3672 Planetary mineralogy and petrology (5410)

Mars, CheMin, X-ray diffraction, Gale crater, aqueous alteration

## 1 Introduction

Gale crater was selected as the landing site for the Mars Science Laboratory (MSL) *Curiosity* rover because of orbital detections of a variety of minerals and diversity of potentially habitable geologic environments in the ancient layered sedimentary rocks that comprise the lower slopes of Aeolis Mons, informally known as Mount Sharp (Golombek et al., 2012). Orbital visible/short-wave infrared (VSWIR) reflectance spectra acquired from portions of lower Mount Sharp by the Compact Reconnaissance Imaging Spectrometer for Mars (CRISM) on the Mars Reconnaissance Orbiter show distinct units containing minerals that likely formed from aqueous alteration, including hematite ($\alpha$-$Fe_2O_3$), smectite, and sulfates (Milliken et al., 2010; Fraeman et al., 2013; 2016). These sediments were deposited ~3.5 Ga ago and may preserve evidence for a dramatic change in climate early in Mars' history. Through analysis of the sedimentology and composition of these units, data collected by *Curiosity* can help characterize the depositional and diagenetic environments and help evaluate differences in these environments that caused the distinct mineralogical changes observed from orbit. Furthermore, quantitative in-situ mineralogical measurements provide ground truth for orbital mineral detections and better constrain the physical surface properties that lead to positive mineral detections from orbit.

Sedimentological observations from images collected by *Curiosity* demonstrate Gale crater was the site of an ancient fluvio-lacustrine environment (e.g., Grotzinger et al., 2014; 2015). *Curiosity* has traversed through over 350 m of vertical stratigraphy since landing in August 2012 (Figure 1). Conglomerate and sandstone on the Gale crater plains are indicative of deposition in fluvial and deltaic environments, respectively (e.g., Williams et al., 2013; Rice et al., 2017), whereas massive and laminated mudstone are markers of deposition in low-energy lake environments (e.g., Grotzinger et al., 2014; 2015). Mudstone deposits are especially

prevalent on the lower slopes of Mount Sharp, and rarity of desiccation features suggests the lakes were long-lived (Grotzinger et al., 2015).

Vera Rubin ridge (VRR) is an erosion-resistant feature on the northern flank of Mount Sharp that was identified from orbit as having a distinct spectral signature of red hematite across much of its length (e.g., Fraeman et al., 2013). The ridge is ~6.5 km long, ~200 m wide, and oriented in a northeast-southwest direction. CRISM spectra of the ridge show pixels that have absorption features near 0.55 and 0.86 μm (consistent with crystalline red hematite), and a lack of hydration features (e.g., at 1.9 μm) demonstrates the ridge is less hydrated than surrounding units (Fraeman et al., 2013; 2016).

The mineral assemblages of samples drilled by *Curiosity* from VRR provide constraints on the ridge's geological history and allow us to test and refine previous hypotheses about its formation. On Earth, for example, hematite forms via different mechanisms and under a variety of conditions, including direct precipitation from Fe-bearing oxic lake waters or hydrothermal fluids, thermal dehydration of crystalline or amorphous Fe oxyhydroxide(s), thermal oxidation of magnetite-bearing lavas, or transformation of amorphous or crystalline Fe oxides and oxyhydroxides in aqueous fluids (e.g., Christensen et al., 2000; Schwertmann and Cornell, 2000). Prior to *Curiosity's* arrival at VRR, hematite on VRR was hypothesized to have formed at a redox interface where aqueous $Fe^{2+}$ was oxidized to $Fe^{3+}$ and precipitated as $\alpha$-$Fe_2O_3$ (e.g., Fraeman et al., 2013; 2016). This oxidation may have occurred in the lake sediments from photooxidation in shallow lake waters, or may have formed by a later diagenetic episode and migration of anoxic $Fe^{2+}$-bearing fluids that mixed with oxidizing fluids or atmosphere. The hematite has also been hypothesized to have formed by mildly acidic alteration of olivine in oxic fluids, causing the precipitation of $Fe_2O_3$ and amorphous silica (Fraeman et al., 2013). The minerals that are found in association with hematite on VRR and their geologic context allow us to test these hypotheses and evaluate the formation mechanisms for these deposits.

Here, we report on the mineral and amorphous abundances from three rock samples drilled from VRR and one from immediately below the ridge, the calculated composition of the amorphous materials, and the unit-cell parameters and crystal chemistry of major phases. We then use the combined mineralogical, geochemical, and sedimentological data to propose a model for the depositional and diagenetic history of VRR.

## 2 Methods

135 *2.1 Vera Rubin ridge campaign*

136 *Curiosity* executed an extensive scientific campaign on the ridge from September 2017 to
137 January 2019, and details of the campaign are reported by Fraeman et al. (*this issue*). In-situ
138 sedimentological observations indicate the ridge is primarily comprised of laminated mudstone,
139 suggesting the sediments were deposited in a lacustrine setting, similar to the conformable
140 sediments stratigraphically below it (e.g., Grotzinger et al., 2015; Edgar et al., *this issue*). The
141 Blunts Point member is directly below VRR, and the Pettegrove Point and Jura members
142 comprise the lower and upper portions of the ridge, respectively. All three members are part of
143 the Murray formation in the Mount Sharp group, which *Curiosity* first began studying in
144 September 2014 with its arrival at the Pahrump Hills outcrop (Figure 1; Grotzinger et al., 2015;
145 Stack et al., 2018). For a detailed description of the sedimentology of VRR, please refer to Edgar
146 et al. (*this issue*).

147 *Curiosity* drilled three mudstone samples on the ridge and one from the Blunts Point
148 member immediately below the ridge (Figures 1, 2, and 3). The successful drilling of the rocks
149 on and just below VRR was especially exciting because an anomaly with the drill feed
150 mechanism on sol 1536 temporarily precluded drilling and delivery of drilled rock samples to the
151 internal laboratories, Chemistry and Mineralogy (CheMin) and the Sample Analysis at Mars
152 (SAM), for over 500 sols. Engineers addressed this anomaly with a new method of drilling called
153 "feed-extended drilling" in which the drill feed remains extended to its full length and is pressed
154 into the rock surface by the rover arm. With feed-extended drilling, a powdered rock sample can
155 no longer pass through the sample handling system on the arm, so it cannot be sieved or
156 portioned by the Sample Acquisition, Processing, and Handling (SA/SPaH) subsystem. Instead,
157 drilled rock samples are delivered to CheMin and SAM by holding the drill bit over an
158 instrument inlet while the drill bit is reversed and vibrated to allow material in the sleeve to drop
159 into the inlet.

160 The return to drilling was marked with a sample called "Duluth" collected from the
161 Blunts Point member on sol 2057 at an elevation of -4192.5 m. The "Stoer" sample was collected
162 on sol 2136 at an elevation of -4169.9 m from the Pettegrove Point member near some of the
163 strongest hematite spectral signatures observed from orbit. The science team attempted to drill
164 samples from Pettegrove Point within the pixels with the deepest hematite-related absorptions in
165 CRISM-based maps, but these locations proved too hard to drill to the optimum sampling depth

of ~4 cm (e.g., Jacob et al., *this issue*). As a result, Stoer came from a region without a strong orbital hematite signature. *Curiosity* drilled two samples from the Jura member. The Jura is heterogeneous in color, with red, gray, and purple tones (Horgan et al., *this issue*). The "Highfield" sample was drilled on sol 2223 at an elevation of -4146.9 m from a gray portion of the Jura, and the "Rock Hall" sample was drilled on sol 2261 at an elevation of -4143.6 m from a red portion of the Jura right before *Curiosity* ended the VRR campaign and descended the ridge to the south.

*2.2 CheMin analyses*

We determined the quantitative mineralogy of drill samples from VRR using *Curiosity's* CheMin instrument. X-ray diffraction (XRD) data from CheMin provide quantitative abundances of well-crystalline phases with a detection limit of ~1 wt.% and quantitative abundances of X-ray amorphous materials with larger errors on their abundance (Blake et al., 2012). CheMin is an X-ray diffractometer (XRD) and X-ray fluorescence (XRF) spectrometer located in the body of the rover (Blake et al., 2012). The instrument uses a Co X-ray source and is in transmission geometry. A collimated X-ray beam is transmitted through a powdered sample in one of 27 reusable sample cells that have Kapton or Mylar windows. Piezoelectric actuators on each pair of sample cells induce convective motion of the sample powder allowing grains in different orientations to be exposed to the beam. Diffracted photons are recorded by an energy-sensitive two-dimensional charge-coupled device (CCD). Data are collected in 30-minute intervals called "minor frames." Samples are typically measured on three separate nights, with 15 minor frames collected each night, for a total of 45 minor frames. The energy of the detected photons produces an XRF spectrum that provides qualitative geochemical data, whereas the position of the detected photons on the CCD produces a 2D XRD pattern. Diffraction rings in the Co-K$\alpha$ 2D pattern are summed circumferentially using a modified version of the GSE_ADA software (Dera et al., 2013) to produce a traditional 1D diffraction pattern.

Each of the four samples collected on and immediately below VRR was analyzed in Mylar cells for 22.5 hours (i.e., 45 minor frames) over three nights for Stoer, Highfield, and Rock Hall and over four nights (but still 45 minor frames) for Duluth. The first sample delivery of Duluth to CheMin did not fill the sample cell, so data collected from the initial night were not used to produce the Duluth XRD pattern. The second delivery filled the cell, and only 6 minor frames were commanded for that first night of analysis. This tactical decision was made to

ensure the cell was filled without wasting instrument consumables. Fifteen minor frames were collected for Duluth on nights two and three, and nine minor frames were collected on the fourth night. Stoer was analyzed in a pristine cell (number 10a) because the CheMin team wanted to minimize cross-contamination for the type sample from VRR. Duluth, Highfield, and Rock Hall were all analyzed in reused cells, after analyses of the emptied cells demonstrated that the cells were free of material from the previous samples. Duluth was analyzed in cell 13b, which previously held the sample John Klein (Vaniman et al., 2014); Highfield was analyzed in cell 10a, which previously held Stoer; and Rock Hall was analyzed in cell 7b, which previously held Big Sky and later Okoruso (Yen et al., 2017).

The quality of grain motion in each analysis is evaluated by counting the number of photons that hit the same pixel on the CCD over the course of one minor frame. Based on experience with previous samples, poor grain motion corresponds to 20 or more pixels with >5 hits and generally produces bright spots on the diffraction rings of the 2D patterns.

The Duluth and Stoer drill powders moved freely in the cell throughout all nights of analysis (Figure 4). Highfield moved very poorly each night of analysis, showing the poorest grain motion of any sample measured by CheMin to date. The Rock Hall drill powder moved well throughout most of the first night of analysis, but showed poor grain motion at the end of the first night and throughout the second and third nights' analyses. Grain motion may have a significant effect on the mineral abundances because a small, perhaps unrepresentative, fraction of the sample may preferentially interact with the beam when the sample is not moving well. To examine the effects of grain motion on mineral abundances, we performed Rietveld refinements on 1D patterns from two samples that showed different grain motion behaviors. Stoer moved well during all three nights of analysis, so we refined the 1D patterns from each night to examine whether mineral abundances vary when grain motion is nominal. A previous mudstone sample drilled from the Murray formation, Marimba, delivered to CheMin on sol 1423, showed poor grain motion for the first two nights of analysis (30 minor frames), then good grain motion for the last two nights of analysis (30 minor frames). We refined the 1D patterns from a portion of the analysis with poor grain motion (minor frames 3-17) and from a portion of the analysis with good grain motion (minor frames 31-45) to test whether the difference in grain motion affected derived mineral abundances. The aim of this test was to evaluate how poor grain motion may

generally affect mineral abundances derived from CheMin data and how this could impact our interpretations of Rock Hall data.

Variations in the machining of the sample cells caused individual cells to be offset from their ideal diffraction position on the order of 10s of micrometers. These offsets have little effect on mineral identification or abundances from Rietveld refinement, but can affect determination of unit-cell parameters. Offsets are corrected using an internal calibration method based on the refined unit-cell parameters of plagioclase feldspar in each sample (Morrison et al., 2018). Briefly, natural plagioclase crystals show a linear relationship between unit-cell parameters ɣ and *c*. CheMin 1D patterns with different offsets from the ideal diffraction position are refined, and the refined plagioclase parameters ɣ and *c* are plotted against those of natural plagioclase samples. The intersection between the line that describes the natural plagioclase ɣ and c parameters and the line that describes the plagioclase ɣ and *c* parameters from the offset CheMin pattern defines the offset of each sample. The calculated offsets for Duluth, Stoer, Highfield, and Rock Hall are -87, -110, -81, and -69 μm, respectively.

Quantitative mineral abundances and refined unit-cell parameters of major phases were determined by Rietveld refinement on the offset-corrected 1D patterns using the MDI Jade program. The scale factor, the full-width at half-maximum (FWHM) term f0, and the exponent/Lorentzian term p0 of each phase were allowed to refine, as were the unit-cell parameters for phases in abundances >~5 wt.%. A linear background was fit, and an amorphous hump was refined using a pseudo-Voigt profile without skewness. Phyllosilicate contributions to the patterns were modeled using overlay patterns of a variety of fully dehydrated smectite (i.e., with d(001) ≈ 10 Å) measured on a laboratory version of CheMin. Six independent refinements were conducted, and the reported mineralogy, refined unit-cell parameters, and crystal chemistry are an average of the independent refinements. Phyllosilicate and X-ray amorphous abundances were quantified using a modified version of the FULLPAT program (Chipera and Bish, 2002; Chipera and Bish, 2013). The modified version for CheMin includes patterns of fully dehydrated smectite (i.e., full $H_2O$ loss without loss of structural OH) and X-ray amorphous materials including basaltic and rhyolitic glass, ferrihydrite, palagonite, and allophane, in addition to common igneous minerals. The phyllosilicate structure was modeled from the (02l) peak in the Duluth pattern using BGMN software (Bergmann, 2005).

Bulk mineralogies of the Duluth, Stoer, and Highfield samples were determined by analyzing the 1D patterns from the sum of all 45 minor frames (Figure 5). The relative abundances of Ca-sulfate minerals (gypsum, bassanite, and anhydrite) were constrained by Rietveld refinement of the 1D pattern from the first night's analysis because gypsum ($CaSO_4 \cdot 2H_2O$) dehydrates to bassanite ($CaSO_4 \cdot 0.5H_2O$) within the relatively warm environment inside the CheMin instrument (Vaniman et al., 2018), and the first night's analysis best represents the Ca-sulfate mineralogy of the original sample. Bulk mineralogy of the Rock Hall sample was determined by analyzing the pattern from the first four minor frames because obvious changes in the pattern were detected after the fourth minor frame (Figure 6) and degradation in grain motion after the 12$^{th}$ minor frame suggest the first four minor frames best represent the mineralogy of the original sample. The chemical composition of the plagioclase in each sample was calculated from the refined unit-cell parameters (Morrison et al., 2018).

The chemical composition of the X-ray amorphous component in each sample was estimated from mass balance calculations using the compositions of the crystalline phases derived from Rietveld refinements and the bulk compositions of samples dumped from the drill bit and measured by the Alpha Particle X-ray Spectrometer (APXS). APXS is mounted on the arm of the rover and uses $^{244}Cm$ sources to analyze rock, loose sediment, or dumped sample using X-ray fluorescence and particle-induced X-ray emission spectroscopy (Campbell et al., 2012). Chemical composition of total crystalline phases is calculated using mineral abundances from Rietveld refinement and phyllosilicate abundances from FULLPAT analyses, with the crystal chemistry of major igneous minerals derived from unit-cell parameters, and the nominal anhydrous chemical formulae of all other minerals (e.g., $CaSO_4$ for bassanite, $Fe_2O_3$ for hematite). The augite composition measured in the martian meteorite EETA79001 was used for the pyroxene composition in samples Duluth and Stoer. A nontronite composition was used for the phyllosilicate composition of Duluth based on SAM data (Nová Ves sample from Novák and Čícel, 1978), and a ferripyrophyllite chemical formula was used for the phyllosilicate composition of Stoer, Highfield, and Rock Hall based on the d(001) position in CheMin XRD patterns (Badaut et al., 1992). For the amorphous compositions reported here, we do not incorporate errors in amorphous and mineral abundances and crystal chemistry of plagioclase derived from unit-cell parameters. The methods for estimating the uncertainties in the amorphous calculations will be the subject of a paper in the near future.

## 3 Results

Analyses of CheMin data from the samples drilled on and just below VRR show that the samples are comprised of igneous minerals, iron oxides and oxyhydroxides, sulfates, phyllosilicates, and X-ray amorphous materials (Figure 7). A carbonate or phosphate phase may also be present in one sample (Rock Hall) from VRR. Here, we report on the specific minerals and their abundances (Table 1), the refined unit-cell parameters of the major phases (Table 2), the plagioclase crystal chemistry calculated from refined parameters (Table 3), and the composition of the amorphous component (Table 4). We also report on the effects of grain motion on the mineralogy derived from Rietveld refinements.

### *3.1 Igneous silicates*

The igneous silicates identified in each sample were feldspar and pyroxene. Plagioclase feldspar is the most abundant igneous mineral in every sample. Plagioclase unit-cell parameters are generally consistent with andesine, with a range from $An_{28(3)}$ in Highfield to $An_{44(7)}$ in Rock Hall. Pyroxene is the next most abundant igneous mineral in each sample. We report total pyroxene abundances because the low angular resolution of CheMin commonly precludes a consistent pyroxene identification (i.e., augite vs. pigeonite vs. orthopyroxene) among the independent refinements. Refinements of Highfield and Stoer, however, resulted in the identification of orthopyroxene as the sole pyroxene in those two samples based on the results from all of the refinements, but the CheMin team cautions that we are not certain of the identification of orthopyroxene because of the low angular resolution of the instrument. Potassium feldspar (var. high sanidine) and quartz are minor to trace constituents of every sample, except for Rock Hall, in which they are absent or below the detection limit of CheMin. We specifically investigated for the presence of olivine in each sample, but it was not present above the detection limit of the instrument.

### *3.2 Iron oxides and oxyhydroxides*

The assemblage of iron oxides and oxyhydroxides (Figure 8) is especially important on and near VRR because of the identification of hematite from orbital visible/short-wave infrared data. CheMin data show that hematite ($\alpha$-$Fe_2O_3$) is present in every sample and is the most abundant iron oxide in the samples Duluth, Stoer, and Highfield. The Stoer sample, from the Pettegrove Point member, has the most hematite of any sample drilled to date (~15 wt.% of the bulk sample). Prior to *Curiosity's* investigation of VRR, the Oudam sample, drilled from the

Murray formation ~250 m stratigraphically below VRR, had the most hematite (~14 wt.% of the bulk sample; Bristow et al., 2018; Achilles et al., *submitted*). The refined *a* and *c* unit-cell parameters of hematite in Duluth and the *a* unit-cell parameter of hematite in Rock Hall are within the 1-sigma error of the nominal hematite structure (i.e., $a$ = 5.038 and $c$ = 13.7772 Å measured from single-crystal diffraction data; Blake et al., 1966). The refined unit-cell parameters of hematite in Stoer are significantly smaller than the nominal hematite structure, the *a* cell parameter for the hematite in Highfield is slightly larger whereas the *c* cell parameter is smaller, and the *c* cell parameter in Rock Hall is smaller. The FWHM of the hematite varies among the samples. We measured the FWHM of the hematite (104) peak of each sample because it is a strong reflection with no interference from peaks of other phases. The FWHM of these peaks was measured with the Jade software, using a beryl-quartz standard measured by CheMin on sol 740 to create an instrument profile calibration curve. The FWHM of the hematite from Duluth is significantly larger than those from the samples collected on VRR (Table 5), and the FWHM of the hematite from the samples collected on VRR are close to the angular resolution of CheMin (FWHM ~0.35 °2θ).

Akaganeite (β-$Fe^{3+}O(OH,Cl)$) is present in trace amounts in Stoer and is the most abundant iron oxide/oxyhydroxide in Rock Hall (~6 wt.% of the bulk). The akaganeite peaks in the Rock Hall XRD pattern were sufficiently strong to refine the akaganeite unit-cell parameters, and the refined parameters are consistent with Cl in the mineral structure (Peretyazhko et al., 2019).

Magnetite is present in Duluth, Stoer, and Highfield in abundances near the CheMin detection limit. The six independent refinements identified magnetite ($Fe_3O_4$) and/or maghemite (γ-$Fe_2O_3$) in these three samples, and the "magnetite" group in Table 1 incorporates both phases. The peaks from these phases were too weak to allow meaningful refinement of the unit-cell parameters, so we cannot define the detailed structure of this phase. Magnetite was not identified in refinements of the Rock Hall pattern.

*3.3 Sulfates and phosphates or carbonates*

Each sample has abundant Ca-sulfate minerals, and the proportions of the different types vary between samples (Figure 9). Bassanite ($CaSO_4 \cdot 0.5H_2O$) is the most abundant Ca-sulfate in Duluth, with minor anhydrite ($CaSO_4$) and gypsum ($CaSO_4 \cdot 2H_2O$) at the detection limit of CheMin. Stoer has equal proportions (within the 1-sigma error) of anhydrite and gypsum, with

bassanite near the detection limit. Anhydrite is the most abundant Ca-sulfate in Highfield, and gypsum and bassanite are present in trace amounts. Anhydrite is the only Ca-sulfate mineral in Rock Hall.

Jarosite ($KFe_3(SO_4)_2(OH)_6$) is present in trace amounts in Stoer and Rock Hall. The jarosite peaks were not sufficiently strong to refine the jarosite unit-cell parameters, but jarosite fit the patterns better than natrojarosite ($NaFe_3(SO_4)_2(OH)_6$) or hydronium jarosite ($H_3OFe_3(SO_4)_2(OH)_6$). Jarosite was not identified in Duluth or Highfield.

Trace amounts of fluorapatite ($Ca_5(PO_4)_3F$) improved the fit to the Rock Hall pattern, although its peaks were not sufficiently strong to refine unit-cell parameters. The most intense fluorapatite peak (at ~37.2 °2θ) is located on a shoulder of a peak from plagioclase, and the other peaks from fluorapatite are not strong enough to affect the pattern, making its presence less certain. Furthermore, the most intense peak of fluorapatite occurs at nearly the same location as the most intense peak of siderite ($FeCO_3$), and siderite similarly fits the shoulder at ~37.2 °2θ. Like fluorapatite, the other peaks from siderite are not strong enough to be detected in the Rock Hall pattern. APXS reported 0.87 wt.% $P_2O_5$ in the drill fines dumped from the drill bit. This would allow for up to ~2 wt.% fluorapatite in the sample, which is consistent with CheMin refinements. SAM reported a $CO_2$ release in Rock Hall that may be consistent with the presence of a carbonate (McAdam et al., *this issue*), which strengthens the argument for siderite. We report fluorapatite in Rock Hall in Table 1, but emphasize that we are not confident in this assignment and siderite instead may be present. Interpretations of the aqueous history of Rock Hall should not hinge upon the presence or absence of either fluorapatite or siderite.

*3.4 Phyllosilicates*

Phyllosilicates are present in each sample. Of these four samples, Duluth has the most phyllosilicate with 15±4 wt.%, and Highfield has the least with 5±1 wt.%. The basal phyllosilicate peak in the Duluth pattern is at 10 Å (Figure 10), consistent with collapsed smectite or illite. The relatively low abundance of $K_2O$ in the APXS measurement of the Duluth dump pile (0.94 wt.%) suggests that the phyllosilicate in Duluth is collapsed smectite, rather than illite (e.g., Bristow et al., 2018). The position of the phyllosilicate (02l) peak is a measure of the compositionally sensitive b-axis of the structure, and the positions of the (02l) peaks in the Duluth, Stoer, and Rock Hall patterns are consistent with a dioctahedral occupancy (Figure 10). The phyllosilicate abundance in Highfield is too low to produce a distinct (02l) peak. Evolved

gas analysis of Duluth from the SAM instrument is consistent with the presence of nontronite based on the temperature of the $H_2O_{(v)}$ release (McAdam et al., *this issue*). Modeling the (02l) peak in Duluth using BGMN software suggests Fe(III) content in the dioctahedral sheet is ~0.66, consistent with nontronite (Supplementary Figure 1). The (02l) peaks in Stoer, Highfield, and Rock Hall are too weak for BGMN model determination of the b unit cell.

The positions of the (001) peaks in the diffraction patterns of the three samples collected from VRR suggest that the phyllosilicates present in those samples are different from the nontronite in Duluth. Their basal spacings are ~9.6 Å, rather than 10 Å (Figure 10). This slightly smaller interlayer spacing could be consistent with a completely collapsed smectite that is devoid of any $H_2O$ in the interlayer site through low-temperature heating (e.g., Komadel et al., 2002; Morris et al., 2009), a smectite altered by acid (e.g., Craig et al, 2014), or the Fe(III)-bearing 2:1 phyllosilicate ferripyrophyllite ($Fe_2Si_4O_{10}(OH)_2$; Bristow et al., 2018). CheMin and SAM data are insufficient to distinguish among these possibilities. The distinctly different (i.e., $H_2O$-poor) phyllosilicate on VRR compared to surrounding units is consistent with the absence of a 1.9 μm hydration band in orbital data from the ridge (Fraeman et al., 2013; 2016).

We considered mixed-layer phyllosilicates as an explanation for the 9.6 Å basal spacing. Nontronite-talc is a mixed-layer phyllosilicate that forms from hydrothermal alteration in seafloor sediments and has been proposed as a Mars-analog phyllosilicate (Cuadros et al., 2013; Michalski et al., 2015). Assuming the nontronite is dehydrated, nontronite-talc would have a basal spacing at ~9.6 Å. SAM EGA data, however, do not support the presence of a trioctahedral phyllosilicate like talc because of the lack of a high-temperature $H_2O$ evolution (McAdam et al., *this issue*).

*3.5 X-ray amorphous materials*

X-ray amorphous materials are significant components of each sample. The modeled positions of the amorphous hump from Rietveld refinements of Duluth, Stoer Highfield and Rock Hall were ~26, ~27, ~25, and ~27°2θ, respectively. For amorphous silicates, the position of the hump is dependent on SiO2 content, where opal-A has a maximum at ~25°2θ and basaltic glass has a maximum at ~30°2θ (e.g., Morris et al., 2015). FULLPAT models indicate about a third to a half of each sample's mass is comprised of X-ray amorphous materials. FULLPAT models primarily used diffraction patterns of rhyolitic glass with minor amounts of ferrihydrite to model the amorphous scattering. Diffraction patterns of X-ray amorphous materials, however,

do not have distinct peaks and can be broadly similar to one another, so the types of amorphous materials used in FULLPAT analyses do not necessarily correspond to the types of X-ray amorphous materials actually present. FULLPAT models also identified opal-CT in the Highfield pattern (Supplementary Figure 2). Opal-CT is paracrystalline (e.g., Smith, 1998) and has reasonably sharp peaks in its X-ray diffraction pattern, so this identification by FULLPAT is more robust than other non-crystalline materials.

X-ray amorphous abundances from FULLPAT and X-ray amorphous abundance minima from mass balance calculations are similar for all four samples. Mass balance calculations demonstrate that the amorphous component in each sample has variable amounts of $FeO_T$, $SiO_2$, $SO_3$, $Al_2O_3$, CaO, and MgO, and that the amorphous compositions vary significantly between samples. For example, the amorphous compositions based on mass balance calculations show that the X-ray amorphous component of Duluth is highly enriched in $FeO_T$ (~22 wt.% of the total amorphous fraction) and depleted in $SiO_2$ (~36 wt.%) compared to the other three samples. The X-ray amorphous component of Stoer is highly enriched in MgO (~11 wt.%), relatively enriched in $SiO_2$ (~57 wt.%), and has no $FeO_T$. Highfield's amorphous component has the highest $SiO_2$ of the samples (~65 wt.%), consistent with the identification of minor amounts of opal-CT and indicative of abundant opal-A, but has the lowest $SO_3$ (~3 wt.%). The amorphous component in Rock Hall has the highest $SO_3$ (~23 wt.%) and the lowest $SiO_2$ (~37 wt.%). Because the calculated amorphous compositions do not take errors into consideration (e.g., errors associated with mineral and amorphous abundances and crystal chemistry), the amorphous compositions reported here should not be considered exact. In reality, the calculated amorphous composition for each sample represents a single composition within a range of potential compositions.

*3.6 Effects of grain motion on mineral abundances*

For the Stoer sample, refinements of the three separate nights of analysis produced mineral abundances that were very similar to the abundances from the refinement of the combined three-night pattern (Supplementary Table 1). All mineral abundances, except for the Ca-sulfate minerals, were within the 2-sigma error reported for the refinement of the three-night pattern, and most mineral abundances were within the 1-sigma error. The variability in Ca-sulfate abundances was expected across the three nights of analysis because of the dehydration of gypsum to bassanite within the CheMin instrument over time (Vaniman et al., 2018).

Refinements of 15 minor frame patterns from the Marimba drill powder demonstrated that grain motion significantly affects abundances of some minerals in the samples. Most mineral abundances between the two patterns were within the 1-sigma errors reported by Achilles et al. (*submitted*), but sanidine, anhydrite, and pyroxene abundances were significantly different (Supplementary Table 2). Refinement of minor frames 3-17 (when grain motion was poor) resulted in significantly less sanidine and pyroxene but more anhydrite, whereas refinement of minor frames 31-45 (when grain motion was good) resulted in significantly more sanidine and pyroxene but less anhydrite. We might expect an increase in anhydrite over time as hydrated $CaSO_4$ dehydrates in the CheMin instrument (although only the gypsum to bassanite transition has been documented so far), but we should not expect a significant decrease over time unless that mineral was preferentially ejected from the cell. We have no reason to suspect that material was ejected over time (e.g., we do not see an increase in the intensity of the peak from the Mylar window), so we hypothesize that differences in grain motion in the Marimba drill powder affected peak intensities and, therefore, mineral abundances in the pattern over time. In the case of Marimba, anhydrite grains may have been immobilized in the center of the cell when minor frames 3-17 were collected to increase the intensity of the anhydrite peaks and increase its abundance in the refinement. This grain sorting may have also occurred during the Rock Hall analysis while minor frames 14-45 were collected (Figure 6). We caution that the reported mineral abundances from samples that showed poor grain motion throughout the analysis (e.g., Highfield) may not accurately reflect the true mineral abundances. It is important to note, however, that although grain motion affects mineral abundances, it does not appear to affect the mineral assemblages that are identified by CheMin.

## 4 Discussion

CheMin XRD data of the three samples drilled from VRR and the sample drilled from immediately below the ridge demonstrate mineralogical diversity across the ridge that could not be appreciated from orbital data alone. In addition to differences in hematite abundances, we see evidence for differences in hematite crystallite size, in the types of iron (oxhydr)oxides present, the sulfate mineralogy, and phyllosilicate structures. This variability in secondary phases may indicate multiple fluid episodes with different pHs, temperatures, and/or water activities were responsible for minerals identified on VRR. Here, we discuss the types of fluids implicated by the mineral assemblages and propose an alteration history for the ridge.

473 *4.1 Mineralogical indicators of aqueous processes*

474 *4.1.1 Hematite*

475 Hematite can form in a variety of environments and from a variety of parent materials on
476 Earth, from hydrothermal deposits in rhyolites (e.g., Seeger et al., 1989) to highly weathered
477 tropical soils (i.e., oxisols; e.g., Schwertmann and Latham, 1986; Fontes and Weed, 1991).
478 Although laboratory conditions do not always mimic natural conditions, laboratory syntheses of
479 hematite provide insight into the aqueous conditions under which it forms. Hematite is typically
480 synthesized by (1) thermal dehydration of crystalline goethite ($\alpha$-FeOOH) at temperatures over
481 ~250 °C, (2) forced hydrolysis in strongly acidic (pH 1-2) $Fe^{3+}$-bearing solutions, or (3)
482 transformation of ferrihydrite in aqueous suspension under weakly acidic to weakly alkaline pH
483 (Schwertmann and Cornell, 2000) or ageing in warm, humid air (e.g., Torrent et al., 1982).
484 Although hematite itself is not diagnostic of a specific formation mechanism, its crystallite size
485 and the mineral assemblage can help infer the process by which it formed.

486 Hematite with relatively small crystallite sizes typically forms from a ferrihydrite or
487 nanophase FeOOH precursor, including goethite, akaganeite, and lepidocrocite (e.g.,
488 Schwertmann and Cornell, 2000; Guo and Barnard, 2013). This transition is common in tropical
489 soils on Earth or from elevated temperatures during burial (e.g., Weibel and Grobety, 1999; Guo
490 and Barnard, 2011). Ferrihydrite is a poorly crystalline hydrated Fe(III) oxyhydroxide that forms
491 nm-scale crystallites from rapid oxidation of $Fe^{2+}$ or rapid hydrolysis of $Fe^{3+}$. It is important here
492 to make the distinction between crystallite size and grain or particle size. Crystallite size refers to
493 a single crystal (i.e., a solid with a regularly repeating atomic arrangement). Grains can be
494 comprised of one or many crystallites. Gray hematite (also called specular or microplaty
495 hematite; Lane et al., 2002) is typically coarser-grained than red hematite, where hematite with
496 grain sizes <~5 μm appear red to the human eye and coarser hematite grains >~5 μm appear
497 black or gray (e.g., Catling and Moore, 2003; Morris et al., *this issue*). Large particles made up
498 of aggregates of ~10-200 nm hematite crystallites can appear gray or black (Madden et al., 2010;
499 Egglseder et al., 2019). Gray hematite has been found to form by many different mechanisms
500 (Catling and Moore, 2003), including crystallization from ferrihydrite in aqueous hydrothermal
501 environments at ~100-200 °C, precipitation in acid-sulfate hydrothermal solutions from the
502 breakdown of jarosite (Golden et al., 2008), vapor phase condensation in fumaroles, and high-
503 temperature oxidation of basalts (e.g., Minitti et al., 2005). Gray hematite has been identified in

banded iron formations, in which it may form from a variety of mechanisms, including transformation from ferrihydrite at low-grade metamorphic temperatures (e.g., Sun et al., 2015) and dissolution of hematite-bearing quartz layers by warm, saline solutions, resulting in the aggregation of hematite nanoparticles into mm-scale hematite bands (Egglseder et al., 2019). The dehydration of large (>1 μm) goethite crystallites, generally at temperatures >80 °C, can produce large hematite crystallites that maintain the acicular goethite morphology (Weibel and Grobety, 1999). The most common formation mechanisms for gray hematite require elevated temperatures, but freeze drying suspensions of hematite nanoparticles in confined spaces can also produce gray hematite (Madden et al., 2010).

CheMin's discovery of abundant hematite in the Highfield sample from a gray outcrop in the Jura member suggests that the hematite in the gray Jura is more coarsely crystalline than other locations on VRR and across *Curiosity's* traverse. This is further corroborated by the Fe-rich mm-sized hexagonal crystals interpreted to be hematite found in Ca-sulfate veins in portions of the gray Jura (L'Haridon et al., *this issue*). Finely ground gray hematite typically produces a red powder (e.g., just as scraping a sample of specular hematite on a streak plate creates a red streak), but the drill fines from Highfield remained gray in images collected by *Curiosity* (Figure 3). Analyses of drilled rock powders in the *Curiosity* rover test bed at the Jet Propulsion Laboratory showed that particles created by *Curiosity's* drill are generally >5 μm in diameter, suggesting the hematite particles in the Highfield drill tailings were not small enough to produce a red color.

The Scherrer equation (e.g., Patterson, 1939) is applied to XRD patterns to calculate crystallite size:

$$\tau = \frac{K\lambda}{\beta cos\theta}$$

$\tau$ = mean crystallite size (diameter)

K = dimensionless shape factor (0.9 for spherical particles)

$\lambda$ = wavelength of the X-ray source (1.79027 Å for CheMin)

$\beta$ = FWHM of the diffraction peak

$\theta$ = Bragg angle of the diffraction peak

The mean crystallite size is inversely related to the FWHM of the diffraction peaks, so smaller crystallite sizes produce XRD patterns with broader peaks. Because of the low angular

resolution of CheMin (~0.35 °2θ), the XRD peaks of crystalline phases would be broad compared to those for patterns measured on laboratory instruments, and we cannot use the Scherrer equation to constrain crystallite sizes larger than ~40 nm. We can apply the Scherrer equation to phases whose peaks are broader than ~0.35 °2θ, like the hematite in Duluth. The FWHM of the hematite (104) peak in the three samples from VRR is close to that of the angular resolution of CheMin, but the FWHM of the hematite (104) peak in Duluth is 0.66(18) °2θ (Table 5). Qualitatively, this difference in FWHM suggests that the hematite in Duluth has a smaller crystallite size than the hematite on VRR. Quantitatively, the Scherrer equation indicates the mean hematite crystallite size in Duluth is ~18 nm, if we assume a spherical crystallite shape. We speculate that the relatively small hematite crystallite size in Duluth implies a nanophase precursor (e.g., ferrihydrite or goethite) that formed at low temperatures. The hematite may have formed larger grains on VRR as a result of warmer temperatures and/or the aggregation of smaller hematite particles in saline solutions.

The deviations from the ideal hematite structure (Blake et al., 1966) in the hematite identified in Stoer, Highfield, and Rock Hall may provide further clues into its formation. Many factors affect the hematite structure, including the speciation and concentration of cationic and anionic substitutional impurities and the discrete particle size, shape, and strain (e.g., see discussion by Morris et al., *this issue*). Cationic substitutions for $Fe^{3+}$ in the structure and/or the introduction of vacancies coupled with $OH^-$ can lead to a smaller unit-cell volume than ideal hematite (e.g., Stanjek and Schwertmann, 1992; Dang et al., 1998; Schwertmann et al., 2000). Studies of synthetic hematite with Al incorporated into its structure demonstrate that Al substitution also introduces OH into the structure. A decrease in the *a* cell parameter correlates to an increase in Al whereas a decrease in the *c* cell parameter correlates to an increase in OH (Stanjek and Schwertmann, 1992). The *c* parameters of the hematite in all four samples are relatively similar to one another and are consistent with the c parameters of unsubstituted natural and synthetic hematite (Morris et al., *this issue*). The *a* cell parameter of the hematite in Stoer is especially small compared to hematite detected in other samples in Gale crater (Morris et al., *this issue*), which could result from Al substitution in the structure. Al is commonly incorporated into hematite in terrestrial soils because of the availability of Al in solution (e.g., Schwertmann et al., 2000), and Al may have been available in diagenetic fluids on VRR from the dissolution of phyllosilicates. Although the *a* and *c* cell parameters for hematite in Stoer are consistent with Al

565 substitution, note that some unsubstituted hematite structures have similarly small cell
566 parameters (Morris et al., *this issue*), so we cannot say with certainty that Al substitution in
567 hematite controls the difference in cell parameters between the VRR samples.
568 *4.1.2 Akaganeite and jarosite*
569 The well-crystalline akaganeite and jarosite detected in the Stoer and Rock Hall samples
570 are indicative of saline, acid-sulfate fluids. Well-crystalline akaganeite forms from the hydrolysis
571 of $Fe^{3+}$ in Cl-bearing solutions under acidic pH (~1-6; Refait and Genin, 1997; Rémazeilles and
572 Refait, 2007; Zhao et al., 2012; Peretyazhko et al., 2016; 2018). It is relatively rare on Earth, but
573 has been found in sulfidic/acidic soils, intertidal marshes or lagoons, hydrothermal brines,
574 volcanic vents, iron meteorites, and iron metal corroded by seawater (e.g., Holm et al., 1983;
575 Buchwald and Clark, 1989; Morris et al., 2000; Holtstam, 2006; Bibi et al., 2011). Akaganeite
576 can form at alkaline pH but has a small crystallite size under those conditions; for instance,
577 akaganeite crystallites formed at pH 8 are 2-6 nm in diameter and produce broad XRD peaks
578 (Deliyanni et al., 2001). The sharp XRD peaks of akaganeite in both Stoer and Rock Hall (Figure
579 5) indicate it is well crystalline, suggesting it formed under acidic conditions (Peretyazhko et al.,
580 2018). Akaganeite commonly forms with hematite, goethite, and/or ferrihydrite (e.g., Johnston,
581 1977; Peretyazhko et al., 2016; 2018). It also transforms to hematite at temperatures of ~250-300
582 °C (Ståhl et al., 2003; Glotch and Kraft, 2008; Fu et al., 2020) and can alter to form hematite or
583 goethite under alkaline conditions (Cornell and Giovanoli, 1990).
584 Jarosite forms from the hydrolysis of $Fe^{3+}$ in $SO_4^{2-}$-bearing solutions at a pH of ~1.5-4
585 (e.g., Driscoll and Leinz, 2005). On Earth, it commonly forms during the aqueous alteration of
586 pyrite ($FeS_2$) and other Fe-sulfates, and is found as a precipitate in acid mine drainage, acid-
587 sulfate soils, acid saline lakes, volcanic fumaroles, and acid leaching solutions in the
588 metallurgical industry (e.g., Johnston, 1977; Kunda and Veltman, 1979; Van Breemen, 1982;
589 Alpers et al., 1992; Morris et al., 2000; España et al., 2005). Jarosite can alter to form hematite in
590 low-temperature acidic or neutral solutions (Barrón et al., 2006; Elwood Madden et al., 2012).
591 The detection of both akaganeite and jarosite in the same samples on VRR can constrain
592 past aqueous environments if we assume they precipitated from the same solution (although we
593 note that the minerals in the samples are not in equilibrium, so the rock was likely affected by
594 different fluids during different episodes and akaganeite and jarosite may not have co-
595 precipitated). Peretyazhko et al. (2016) synthesized akaganeite and natrojarosite from hydrolysis

of an $Fe^{3+}$-bearing solution with 0.1 M $SO_4^{2-}$ and a S/Cl molar ratio of 0.17 at pH 1.5. Increasing the pH resulted in the precipitation of hematite and goethite, and decreasing the $SO_4^{2-}$ concentration precluded the precipitation of natrojarosite. Akaganeite and jarosite were found together on andesitic boulders in streams with pH 1-2 near White Island volcano on New Zealand's North Island (Johnston, 1977). Bibi et al. (2011) reported the co-occurrence of akaganeite and jarosite in sulfide-bearing freshwater inlands in New South Wales, Australia. These surface waters had 0.03 M $SO_4^{2-}$, a S/Cl molar ratio of 0.007, and a pH of 2. These studies suggest the coprecipitation of akaganeite and jarosite occurs in solutions with a pH of 1.5-2 with a $SO_4^{2-}$ concentration of 0.03-0.1 M, but they do not help constrain $Cl^-$ concentration.

*4.1.3 Ca-sulfate*

The type of Ca-sulfate mineral present can be used as an indicator of salinity, temperature, and hydrologic conditions. Anhydrite and gypsum are the most common forms of Ca-sulfate on Earth and are usually found in evaporite deposits (e.g., Buick and Dunlop, 1990), but anhydrite is reported in hydrothermal environments (e.g., Sleep, 1991; Hannington et al., 2001). Bassanite is rare on Earth because it is a metastable phase at Earth's surface conditions (e.g., Van Driessche et al., 2017), but it is stable on the surface at Gale crater, where temperatures reach up to 12 °C and relative humidity is <2% during the day (e.g., Rapin et al., 2016; Vaniman et al., 2018). Thermodynamic calculations and solubility measurements indicate that anhydrite precipitates from dilute sulfate solutions at slightly elevated temperatures (~40-60 °C) compared to gypsum, but anhydrite can form from concentrated brines at lower temperatures (e.g., Hardie, 1967; Dixon et al., 2015; Miller et al., 2016; Miller, 2017). Anhydrite can be difficult to precipitate in the laboratory at relatively low temperatures because of slower reaction kinetics than gypsum and bassanite, but it has been synthesized by transformation of gypsum or bassanite in saline solutions similar to those found in terrestrial sedimentary environments at temperatures ≥80 °C (Ostroff, 1964; Ossario et al., 2014). Anhydrite has been successfully synthesized at low temperatures in flow-through jarosite dissolution experiments in $CaCl_2$ brines, whereas gypsum and bassanite were only precipitated in batch reactor dissolution experiments (Dixon et al., 2015; Miller et al., 2016; Miller, 2017). These results suggest anhydrite can be a marker of open hydrologic conditions. Laboratory experiments demonstrate that the precipitation of gypsum vs. bassanite is controlled primarily by salinity, where bassanite forms at lower water activity than gypsum (Cruft and Chao, 1970; Ossario et al., 2014).

The differences in relative abundances of anhydrite, bassanite, and gypsum in Duluth, Stoer, Highfield, and Rock Hall suggest differences in the salinity of the fluids, the duration of fluid activity, fluid flow, and possibly temperature. The Ca-sulfate minerals in Duluth are dominated by bassanite and anhydrite, with very little gypsum, suggesting precipitation of Ca-sulfate from relatively saline fluids or transition from gypsum during extended aqueous activity. It is important to note, however, that Duluth was delivered to CheMin 12 sols after drilling, compared to six sols for Stoer and five sols for Highfield and Rock Hall, and gypsum may have dehydrated to bassanite while in the drill bit (e.g., Vaniman et al., 2018). The presence of abundant gypsum and anhydrite in Stoer and Highfield may suggest multiple fluid episodes; gypsum may have precipitated from fluids with higher water activity and/or closed hydrologic conditions, and anhydrite may have precipitated from fluids with lower water activity, under higher flow conditions, or may have transformed from gypsum in contact with saline fluids. The dominance of anhydrite in Rock Hall may be a marker of saline fluids, longer lived aqueous activity to allow for the transition of gypsum and/or bassanite to anhydrite, an open hydrologic system in the presence of saline fluids, or slightly elevated temperatures >~60 °C. The presence of light-toned fractures in all targets indicates at least some of the Ca-sulfate is a late-stage diagenetic product. We cannot rule out the presence of Ca-sulfate in the matrix, and the observation of swallowtail-shaped crystal molds in the gray Jura suggests gypsum precipitation during deposition or early diagenesis (L'Haridon et al., *this issue*). Therefore, some of the Ca-sulfate detected by CheMin may have also formed as the sediments lithified during early diagenesis.

*4.1.4 Phyllosilicates*

Phyllosilicates are especially important indicators of aqueous alteration on ancient Mars because they are recognized across the planet from orbital VSWIR spectral data (e.g., Bibring et al., 2006; Ehlmann and Edwards, 2014; Carter et al., 2015). X-ray diffraction data from CheMin allow us to investigate the phyllosilicate structures and crystal chemistry to characterize the specific aqueous conditions under which they formed. CheMin and SAM data from Duluth are consistent with the presence of nontronite, a dioctahedral smectite. Nontronite commonly forms on Earth from hydrothermal alteration or weathering of mafic minerals in soils (e.g., Sherman et al., 1962; Meunier, 2005). Two of the common nontronite standards from the Clay Minerals Society, NAu-1 and NAu-2, formed from hydrothermal alteration of biotite and amphibole in

schist, gneiss, and amphibolite (Keeling et al., 2000). Nontronite is also found in basaltic soils with leaching under anoxic conditions to allow for the release of Fe from mafic minerals and to maintain $Fe^{2+}$ in solution (e.g., Sherman et al., 1962; Baker and Neill, 2017). Nontronite decomposes to Fe-oxides over time by desilication in these soils. Nontronite generally forms in poorly drained soils, and the transition to well-drained soils promotes formation of aluminous clay minerals, including montmorillonite and kaolinite (e.g., Baker and Neill, 2017). The oxidation of synthetic ferrous smectite can lead to the formation of nontronite and the concomitant precipitation of nanophase hematite from the ejection of $Fe^{3+}$ from the nontronite structure (Chemtob et al., 2017). Nontronite has also been synthesized at relatively low temperatures between 3 and 150 °C (Harder, 1976; Decarreau et al., 2008). These syntheses require a ferrous starting material, reducing conditions, and relatively low dissolved silica to prevent the precipitation of Fe-oxides and amorphous silica. Nontronite can be synthesized at much higher temperatures of ~350 °C with ferric starting materials (e.g., Kloprogge et al., 1999). Ferripyrophyllite, which may be present on VRR based on d(001) = 9.6 Å observed in the Stoer, Highfield, and Rock Hall XRD patterns, has been identified in sediments from the Red Sea that experienced early diagenesis at temperatures 55-65 °C (Badaut et al., 1992).

The phyllosilicate species identified in the samples from and just below VRR are suggestive of relatively intense aqueous alteration compared to previous samples drilled from older strata in Gale crater. Mudstone samples from the base of the stratigraphic section investigated by *Curiosity* in the Yellowknife Bay formation contain Fe-substituted saponite, a trioctahedral smectite (Treiman et al., 2014; Vaniman et al., 2014). The presence of $Fe^{2+}$- and Mg-bearing smectite requires abundant basic cations in solution and relatively low Eh (e.g., Vaniman et al., 2014). Smectite detected by CheMin and SAM in the Murray formation below the Blunts Point member and the location of the Duluth drill hole is a mix of trioctahedral and dioctahedral structures, but becomes increasingly dioctahedral up section (Bristow et al., 2018). This mineralogical change is coupled with a geochemical change that suggests more intense open system alteration up section (Mangold et al., 2019). The nontronite in Duluth is the first fully dioctahedral smectite detected by *Curiosity* and suggests a lower concentration of basic cations in solution (perhaps from leaching) and more oxidizing conditions than the solutions responsible for smectite formation lower in the section. Orbital VSWIR data of phyllosilicate-bearing terrains on Mars suggest ~75% of all smectite detected has high or very high Fe

(Michalski et al., 2015). The high-Fe dioctahedral smectite detected at Duluth may be structurally and chemically similar to high-Fe smectite detected elsewhere on Mars.

Ferripyrophyllite is also a dioctahedral phyllosilicate. If ferripyrophyllite is present on VRR, natural formation conditions imply it formed under warm temperatures (~60 °C) and acidic pH. Bristow et al. (2018) identified ferripyrophyllite based on the 9.6 Å basal peak in a sample from the Murray formation called Oudam previously analyzed by CheMin. They speculated it was detrital, but the discovery of a similar mineral assemblage on VRR and the evidence for diagenesis on VRR suggests it may have formed in situ in both locations. Alternatively, the 9.6 Å basal peak in VRR samples may be from a smectite altered by acidic fluids (Craig et al., 2014), in which case warm temperatures are not necessary but relatively intense alteration is inferred. Data from CheMin and SAM cannot help us distinguish between ferripyrophyllite and acid-altered smectite on VRR, but both suggest the rocks of VRR experienced a higher degree of alteration than surrounding units. Ferripyrophyllite has not been detected from orbit on Mars, perhaps because no one has looked for this particular mineral. We recommend the clay mineralogists and spectroscopists in the Mars community consider the presence of ferripyrophyllite when considering mineralogical assignments from CRISM spectra.

The alteration of preexisting phyllosilicates may also be tied to the precipitation of Fe-oxides and oxyhydroxides and opaline silica. Conformable units below VRR and the Blunts Point member contain abundant smectite (Bristow et al., 2018), and units that are stratigraphically equivalent to Jura in the Glen Torridon locale to the south of VRR contain the most smectite observed to date (Bristow et al., 2019). Fe-bearing smectite alteration on VRR could result in a relatively low abundance of phyllosilicate on VRR, in addition to precipitation of Fe-oxides and oxyhydroxides from the Fe present in the smectite structure and the precipitation of opaline silica from leaching of silica from clay mineral tetrahedral layers (e.g., Sherman et al., 1962; Chemtob et al., 2017).

*4.1.5 X-ray amorphous materials*

The identification of opal-CT in the Highfield XRD pattern suggests a diagenetic origin from the transformation of opal-A. On Earth, silica typically matures in sedimentary environments during early diagenesis from opal-A → opal-CT → cryptocrystalline quartz, and opal-CT forms from opal-A through a dissolution-reprecipitation reaction (e.g., Kastner et al., 1977). Opal-CT is common in deep sea sediments, where the silica is usually sourced from

siliceous ooze, in silica sinters from hot springs, where the silica is from hydrothermal alteration of volcanic rocks, and in volcanic rocks that have experienced early diagenesis (e.g., Riech and von Rad, 1979; Altaner and Grim, 1990; Lynne and Campbell, 2004). The transformation from opal-A to opal-CT typically occurs at slightly elevated temperatures (~18-56 °C), but it has been observed at much colder temperatures (0-4 °C) in shallowly buried Antarctic deep-sea sediments (Botz and Bohrmann, 1991).

The composition of the X-ray amorphous components in each sample may also hold clues for the nature of aqueous solutions that interacted with the sediments in ancient Gale crater. Although FULLPAT analyses modeled much of the amorphous component in each sample as volcanic glass, none of the calculated amorphous chemical compositions is consistent with a volcanic glass composition. Glass could be a constituent of the amorphous materials, but the variable enrichment in $SiO_2$, $FeO_T$, and $SO_3$ suggests a secondary origin for at least a portion of the amorphous component. The concentration of $SO_3$ in the amorphous component of all samples, particularly Rock Hall, indicates the presence of amorphous sulfates (e.g., Vaniman et al., 2004). XRD patterns of amorphous Fe- and Mg-sulfates are similar to those of volcanic glass (Morris et al., 2015), and SAM evolved $SO_2$ emissions indicate the presence of Mg sulfate in all samples and Fe sulfate in all samples except Highfield (McAdam et al., *this issue*). The lack of Fe in the amorphous component in Stoer and the elevated MgO inferred from mass balance calculations suggest that all Fe-sulfate in Stoer is crystalline (i.e., jarosite) and the amorphous sulfate is magnesian. The combined SAM and CheMin data indicate the presence of amorphous Mg-sulfate in Duluth, Stoer, Highfield, and Rock Hall and amorphous Fe-sulfate in Duluth and possibly Rock Hall. These amorphous sulfates may have formed by rapid precipitation from the evaporation or freezing of sulfate-bearing fluids, and the very high abundance of $SO_3$ in the Rock Hall amorphous component suggests those fluids were particularly concentrated in $SO_4^{2-}$.

Elevated concentrations of $SiO_2$ in the amorphous component of Stoer and Highfield, the position of the X-ray amorphous hump, and the detection of opal-CT by FULLPAT in Highfield indicate the presence of opaline silica in these two samples. The presence of opal suggests precipitation of silica from solution, which could have been mobilized at elevated temperature, elevated pH, or by the dissolution of other silicates, like mafic silicates or clay minerals (e.g., Iler, 1979; McLennan, 2003).

The especially high concentration of $FeO_T$ in Duluth suggests an amorphous Fe phase, like two-line ferrihydrite, is abundant just below VRR. The presence of ferrihydrite-like materials suggests rapid hydrolysis of $Fe^{3+}$ in solution (e.g., Schwertmann and Cornell, 2000). $Fe^{3+}$ can be mobilized in solutions with extremely acidic pH. Alternatively, the amorphous Fe phase may have formed by rapid oxidation of $Fe^{2+}$ in solution followed by $Fe^{3+}$ hydrolysis, which would imply that reducing conditions mobilized Fe. A ferrihydrite-like phase may also be present in Highfield and Rock Hall, although the $FeO_T$ in the amorphous component in Rock Hall may be associated with the elevated $SO_3$ in that sample.

The abundance of amorphous materials in all VRR samples is also important to consider when constraining the diagenetic history of the ridge. Amorphous materials in rocks and soils on Earth commonly mature to crystalline phases as a result of aqueous alteration and diagenesis (e.g., opaline silica matures to quartz, and ferrihydrite matures to hematite or goethite; e.g., Kastner et al., 1977; Schwertmann and Cornell, 2000), although amorphous materials have been recognized in ~30 Ma old paleosols (Smith et al., 2018). The presence of opaline silica and nanophase Fe-oxides/oxyhydroxides on VRR indicates that, although aqueous alteration may have been relatively intense on the ridge, fluids may not have been sufficiently long-lived to allow for the maturation of amorphous materials (e.g., Tosca and Knoll, 2009).

*4.2 Conceptual model to explain the mineral assemblages on Vera Rubin ridge*

Any conceptual model to explain the history of Vera Rubin ridge must account for variations in hematite crystallite size on and just below the ridge, detection of akaganeite and jarosite in Stoer and Rock Hall, phyllosilicate with d(001) = 9.6 Å on the ridge, presence of opal-CT in Highfield, differences in Ca-sulfate mineralogy, and formation of the erosion-resistant ridgeline. Without petrography and knowledge of the textural relationships between minerals at the grain scale, it is difficult to identify a sequence of events and characterize each phase as detrital or authigenic. Although the model we put forward is consistent with *Curiosity's* results, it is certainly not the only model that can explain the observations, and other reasonable models are presented in other papers in this issue. Below, we present a model to explain the mineralogy and sedimentology from sediment deposition through late diagenesis and erosion to the current topography (Figure 11).

The generally small grain size and fine laminations of the rocks on the ridge indicate deposition of sediments in a lacustrine environment (Edgar et al., *this issue*). Feldspar and

pyroxene were likely detrital inputs, and the variation in plagioclase composition may indicate different sources or may result from local variations in alteration intensity. Ca-rich plagioclase is more susceptible to alteration than Na-rich plagioclase (e.g., Lasaga, 1984), and the low anorthite number for the plagioclase in Highfield may point to more intense alteration in that sample. We speculate that Fe-substituted saponite formed relatively early in the history of the ridge, either as detrital input or as an authigenic phase (e.g., similar to early diagenetic smectite formation hypothesized at the base of the Gale crater section; McLennan et al., 2014; Vaniman et al., 2014; Bristow et al., 2015). The minerals and amorphous materials discovered in the Duluth, Stoer, Highfield, and Rock Hall samples imply localized alteration of these lacustrine sediments under variably acidic and saline conditions and slightly elevated temperatures. Because of the presence of abundant $FeO_T$ in the amorphous component of Duluth and the implication of small hematite crystallite sizes from the large FWHM, we propose that the hematite found on VRR and throughout much of the Murray formation below VRR formed from a ferrihydrite-like precursor. The ferrihydrite-like material could have formed at the sediment-water interface or in the near subsurface, while the lake waters were present, from the oxidation of $Fe^{2+}$ followed by $Fe^{3+}$ hydrolysis. $Fe^{2+}$ could be released into solution from alteration of mafic igneous minerals, like pyroxene and olivine, or of $Fe^{2+}$-bearing smectite (e.g., Chemtob et al., 2017). It may also have formed during diagenesis and the alteration of $Fe^{2+}$-bearing minerals by groundwater.

We hypothesize that much of the alteration and the precipitation of many of the secondary phases occurred after lithification during multiple late diagenetic episodes because of the geologic evidence for late diagenesis across *Curiosity's* traverse and because the mineral assemblages are not in equilibrium, suggesting different aqueous conditions and relatively short-lived aqueous events. Diagenesis in terrestrial sedimentary basins is notoriously complex, where a number of variables (e.g., the structure of the basin, permeability of units, composition of diagenetic fluids, number of diagenetic events) controls mineralogical variations on the micro- to basin-scale (e.g., Elmore et al., 2016; Egenhoff, 2018). The differences in mineralogy across VRR and between stratigraphically equivalent units on VRR and Glen Torridon suggest diagenesis played a significant role in the history of VRR. The non-equilibrium assemblage could also suggest that the secondary components formed elsewhere and are detrital, but we favor in-situ formation through multiple fluid events because of the visual and compositional evidence for late diagenesis in Gale crater.

Although there is a general lack of element mobility across VRR (Thompson et al., *this issue*), there is evidence on VRR and throughout the Murray formation for fluids moving along geologic contacts and within fractures post lithification. Loss of Mg, Al, Mn, Fe, Ni, Zn, and other elements was recognized in fracture-associated halos in the Stimson formation (Yen et al., 2017), an eolian sandstone that unconformably overlies the Murray formation (Banham et al., 2018). These halos extend into the Murray formation, particularly at a location called Marias Pass, where there is a beautiful exposure of the Stimson and Murray contact. Depletion of basic cations along the fractures suggests leaching from fluids with variable pH (Yen et al., 2017; Hausrath et al., 2018). Bright-toned deposits have been recognized elsewhere along the Murray-Stimson contact, suggesting deposition of secondary materials from fluids. Abundant Ca-sulfate bearing veins observed along the traverse suggest late-stage $SO_4^{2-}$-bearing solutions (Nachon et al., 2014; Rapin et al., 2016; VanBommel et al., 2016; L'Haridon et al., 2018). Complex veins, including the Ronan target on VRR (Kronyak et al., 2019) and the Garden City outcrop near Marias Pass (Berger et al., 2017; VanBommel et al., 2017), imply multiple late fluid episodes. Some fractures near the top of VRR are especially unique, containing a Ca-sulfate matrix and euhedral Fe-rich crystals consistent with hematite along with halos in the surrounding mudstone (L'Haridon et al., *this issue*). A quantitative measure of relatively young diagenetic fluids is the age of the jarosite measured from K-Ar analysis of the Mojave2 target in the Pahrump Hills section of the Murray formation (2.12±0.36 Ga; Martin et al., 2017). Although there is some evidence for localized elemental mobility along fractures within VRR rocks (L'Haridon et al., *this issue*; David et al., *this issue*), the bulk chemistry of rocks on VRR does not differ from the bulk chemistry of the rocks measured in other parts of the Murray formation (Thompson et al., *this issue*). The lack of elemental mobility across the ridge suggests that aqueous alteration during diagenetic episodes occurred at a relatively low water-to-rock ratio and/or occurred in a closed system. Hydrous alteration models indicate alteration at VRR, however, occurred at a higher water-to-rock ratio than at the base of the section in Yellowknife Bay (Turner et al., *this issue*).

Vera Rubin ridge lies near the base of the Greenheugh pediment capping unit (Figure 12), which is an unconformable unit that is part of the Siccar Point group (Fraeman et al., 2016). The contact between the Murray formation and the overlying Siccar Point group (which includes the Stimson formation and Greenheugh pediment capping unit; Fraeman et al., 2016; Bryk et al.,

2019) may have provided a pathway for late diagenetic fluids. Although the Siccar Point group sediments in the Greenheugh capping unit are not in direct contact with VRR, projection of the capping unit based on regional dips places it directly on top of VRR, from which it may have since eroded (Bryk et al., 2019). After lithification, fracturing, and erosion of the Murray formation and the deposition and lithification of the Siccar Point group sediments, we speculate that episodic warm, acidic, and/or saline fluids moved along the contact, where the change in rock properties may have permitted a conduit. Unconformities in sedimentary basins on Earth can serve as conduits for warm diagenetic fluids, resulting in higher temperatures of alteration along the contact than would be expected from burial diagenesis and the regional geothermal gradient (e.g., Harper et al., 1995; Laverret et al., 2006; Chi et al., 2015).

There are a few hypothetical sources of heat in Gale crater. The warm fluids that interacted with portions of VRR may have been sourced from burial diagenesis and associated thermally driven fluid convection. These warm fluids would have been transported from depth along vertical fractures, then flowed horizontally or subhorizontally along contacts or more permeable units. Burial diagenesis in Gale crater may have produced temperatures up to 125 °C in rocks that are currently exposed at the surface (Borlina et al., 2015), and buried sediments likely extend another 2 km below the floor of the crater (Grotzinger et al., 2015). This suggests burial diagenetic temperatures in the lowest strata of the Gale crater sedimentary basin may have exceeded 125 °C. We favor warm fluids causing the precipitation of gray hematite on VRR because elevated temperatures are typically required for gray hematite formation on Earth, but other low-temperature mechanisms may have led to the precipitation of gray hematite. Specifically, Ostwald ripening, during which small particles are dissolved and reprecipitated as larger particles, may have transformed red hematite to gray hematite on VRR and may explain coarse-grained hematite detected at Meridiani from orbit and in situ (Glotch and Kraft, 2008). This process could have occurred at relatively low temperatures, but would require fluids to persist for longer periods of time. In this scenario, groundwater would have been transported preferentially along the contact between the Murray formation and Siccar Point group, but it would not have been warm.

Alternatively, warm fluids may have been sourced from geothermal plumes, in which groundwater was warmed at depth (perhaps from regional shallow magmatism infiltrating into fractures in the crust underlying Gale crater) and ascended as a result of its relative buoyancy.

Seismic data collected by the Insight lander from Elysium Planitia ~600 km north of Gale crater indeed indicate the upper 8-11 km of the martian crust is heavily fractured and/or altered (Lognonné et al., 2020). Elysium Planitia is the site of some of the most recent volcanism on Mars, with lava flows dating to 2-250 Ma from crater counts (Vaucher et al., 2009). Modern seismic activity detected by InSight furthermore suggests that the interior is still moderately active (Banerdt et al., 2020). Numerical models of hydrothermal fluid circulation in bedrock surrounding magmatic intrusions and sills indicate warm, circulating groundwater can extend hundreds of meters to kilometers from the heat source (e.g., Gulik, 1998; Iyer et al., 2013). Models that incorporate weakly permeable layers within more permeable bedrock indicate fluids may extend further from the heat source along the contact with these weakly permeable layers (Gulik, 1998). With the high smectite abundance in much of the Murray formation, the Murray may have been weakly permeable compared to the overlying Siccar Point group rocks, creating a conduit for warm groundwater.

A final potential source of heat in the Gale crater basin is radiogenic heat from the decay of $^{40}K$, $^{238}U$, $^{235}U$, and $^{232}Th$ in the sediments. The half-lives of these unstable isotopes are sufficiently long to provide heat to sediments deposited in the basin for billions of years (e.g., the half-lives of $^{40}K$ and $^{232}Th$ are 1.3 and 14.1 Ga, respectively). *Curiosity* does not have the ability to measure U and Th, but both have been detected on Mars via orbital gamma-ray spectroscopic data (e.g., Boynton et al., 2007) and in martian meteorites (e.g., Meyer, 2003). U and Th abundances and have been used to calculate radiogenic heat flux in the martian crust (e.g., Hahn et al., 2011) and were accounted for in the burial diagenetic models by Borlina et al. (2015). *Curiosity* can quantify K abundances with APXS and laser-induced breakdown spectroscopy on ChemCam. Geochemical data from APXS and ChemCam show that Gale crater sediments are enriched in $K_2O$ relative to average Mars crust. The average Mars crust has 0.45 wt.% $K_2O$ (Taylor and McLennan, 2009), whereas the Murray and Bradbury formations have averages of approximately 1 wt.% $K_2O$, with maximum concentrations of 4 wt.% in APXS data and over 11 wt.% in ChemCam data from the Bradbury (e.g., Le Deit et al., 2016; Siebach et al., 2017; Bedford et al., 2019; Mangold et al., 2019). The excess $K_2O$ in Gale crater sediments could provide an additional source of heat in this basin. Future work should examine these potential heat sources and model the diagenetic fluid temperatures that could be achieved in each scenario to determine which heat source is most consistent with the mineralogical observations.

Acidic fluids may have been sourced from the dissolution and oxidation of Fe-sulfides (e.g., Nordstrom, 1982). The acidic fluids would have been neutralized by the consumption of $H^+$ during the dissolution of mafic minerals (e.g., pyroxene), potentially causing large pH gradients and explaining the intermittent precipitation of minerals that precipitate from acidic fluids (i.e., jarosite and akaganeite).

These late-stage diagenetic fluids facilitated the crystallization of amorphous ferrihydrite-like material to hematite. Where the fluids were locally warmer, larger hematite crystallites (i.e., gray hematite) would have formed. Acidic fluids could have altered preexisting smectite to make them more susceptible to enhanced structural collapse, giving rise to the d(001) = 9.6 Å observed in the Stoer, Highfield and Rock Hall patterns (e.g., Craig et al., 2014), or warm acid-saline fluids could have led to the precipitation of ferripyrophyllite (e.g., Badaut et al., 1992). Alteration of Fe-bearing saponite on VRR under oxidizing conditions could have caused the oxidation of $Fe^{2+}$ and the ejection of $Fe^{3+}$ from the octahedral sites of smectite and dissolution of silica from clay mineral tetrahedral sheets to contribute to the crystallization of hematite and precipitation of opaline silica, respectively (Chemtob et al., 2017). Hematite and amorphous silica may be the materials cementing the sediments on VRR, making them relatively resistant to erosion and forming a ridge. Evaporation (if sediments were in communication with the atmosphere), cooling, and/or possibly freezing of the fluids would have lowered the solubility of salts in solution and may have concentrated the acid-saline fluids in pockets, causing precipitation of akaganeite and sulfates. Evolution of the fluid compositions with cooling/freezing and the changes in saturation indices for different minerals could result in mineralogical heterogeneities at small spatial scales. The assemblage in Rock Hall might represent one of these concentrated pockets of acid-saline solutions, where abundant akaganeite and anhydrite and minor jarosite precipitated. Mastcam multispectral data of Rock Hall and other red Jura targets demonstrate that Rock Hall is an outlier in the red Jura, further suggesting the acid-saline fluids that altered the Rock Hall target were localized (Horgan et al., *this issue*). The relative timing of the formation of hematite in Stoer and Highfield and akaganeite in Rock Hall is unconstrained. Both minerals could have formed contemporaneously from a ferrihydrite-like precursor, but under different local aqueous conditions, or akaganeite could have been more widespread on the ridge and altered to red and gray hematite from further aqueous alteration on portions of VRR.

This late-stage diagenesis potentially along the contact between the Murray formation and the Siccar Point group also explains mineral assemblages of drill samples lower in the Murray. The mineralogy of the Sebina, Quela, and Marimba samples drilled ~100-200 m stratigraphically below Duluth is dominated by plagioclase, hematite, Ca-sulfate, and smectite with trace amounts of jarosite (Bristow et al., 2018). These samples have more smectite than the samples on VRR, but slightly less (red) hematite, so they may have experienced diagenesis by lower-temperature and less acidic fluids such that gray hematite did not precipitate and the smectite was not altered. The diagenetic episode(s) that caused crystallization of hematite on VRR may have been contemporaneous with the episode(s) that caused the crystallization of hematite stratigraphically below VRR. The mineralogy of the Oudam sample, drilled ~250 m below Duluth, is much like that of Highfield, with abundant gray hematite and plagioclase, minor opal-CT, but small amounts of phyllosilicate with d(001) = 9.6 Å (Bristow et al., 2018; Achilles et al., *submitted*). These sediments at Oudam may have also experienced diagenesis by warm, acidic fluids and indicate that warm fluids were not limited to VRR. The presence of a resistant ridge at VRR, however, suggests these diagenetic fluids may have been more widespread at VRR.

## 5 Conclusions

CheMin XRD analyses of mudstone samples collected from VRR suggest a complex aqueous alteration history and confirm the orbital detection of hematite. The concentration of hematite on VRR varies in the three samples collected, comprising ~3-15 wt.% of the bulk material. The Stoer sample had the most hematite of any sample drilled to date, but it was not drilled from a portion of the ridge with a strong orbital hematite spectral signature, suggesting physical properties of the surface control hematite detection from orbit (Fraeman et al., *this issue*). The identification of abundant hematite in some samples stratigraphically below VRR from surfaces that did not show strong orbital hematite signatures (e.g., Bristow et al., 2018) further demonstrates that hematite concentration is not the only factor that controls its detection from orbit. The relatively low abundances of phyllosilicates on VRR compared to surrounding units (e.g., Bristow et al., 2018) are consistent with the relatively weak hydration features observed from orbit (Fraeman et al., 2013; 2016).

The mineralogical information from CheMin suggests multiple episodes of variably warm, saline, and/or acidic fluids preferentially altered the rocks on VRR. The detection of gray

hematite in the Highfield sample from the gray Jura member is the strongest evidence for warm fluids because it commonly forms from alteration at 100-200 °C (Catling and Moore, 2003). The presence of a 9.6 Å phyllosilicate peak in all samples from VRR and opal-CT in Highfield also suggest preexisting smectite was altered by the diagenetic fluids. Jarosite and well-crystalline akaganeite in the Stoer sample from the Pettegrove Point member and the Rock Hall sample from the red Jura member are both indicative of acidic fluids with low water activity. The high abundance of anhydrite in Rock Hall in particular is further evidence for waters with high ionic strength. Because of some mineralogical similarities between samples from VRR and those collected lower in the Murray formation (i.e., abundant hematite, phyllosilicate, and Ca-sulfate; Achilles et al., *submitted*), we suggest the late-stage diagenetic fluids that altered rocks on VRR may have also altered other portions of the Murray formation, but alteration was most intense along VRR. The abundant and, in some locations, coarse-grained hematite and hypothesized alteration of smectite to precipitate opaline silica may have made the rocks of VRR more resistant to physical weathering compared to underlying units. In our proposed scenario, poorly crystalline $Fe^{3+}$ oxyhydroxides (e.g., ferrihydrite) precipitated from lake waters while the Murray formation was being deposited. After lithification and erosion of the Murray and the deposition and lithification of the uncomformably overlying Siccar Point group, variably warm, acidic, saline fluids moved along the contact between the two units during multiple episodes. These diagenetic fluids caused crystallization of gray hematite where the fluids were warmer and red hematite where the fluids were relatively cool. They could have altered preexisting smectite to precipitate ferripyrophyllite, amorphous and paracrystalline silica, and hematite on the ridge, but cooler, less acidic fluids would not have had a significant impact on the smectite. Akaganeite, jarosite, and Ca-sulfate would have precipitated where these fluids accumulated and became concentrated through evaporation or freezing. *Curiosity* is currently studying a smectite-bearing unit identified from orbit and is approaching a contact between the Murray formation and Siccar Point group. Studying the composition and sedimentology of the rocks at, above, and below the contact will allow the science team to test the hypothesis that the contact served as a conduit for diagenetic fluids.

## 6 Acknowledgements

We gratefully acknowledge the MSL engineering, management, and tactical and strategic operations teams who facilitated data collection during the VRR campaign. Reviews by J.

Bridges, K. Cannon, N. Mangold, S. VanBommel, and two anonymous reviewers greatly improved the manuscript. CheMin XRD data presented in this paper are archived in the Planetary Data System (PDS) and the CheMin Open Data Repository (ODR). Within the PDS, the Duluth 1D diffraction pattern can be found here: https://pds-geosciences.wustl.edu/msl/msl-m-chemin-4-rdr-v1/mslcmn_1xxx/data/rdr4/cmb_581124537rda20690701752ch00111p1.csv, the Stoer 1D diffraction pattern can be found here: https://pds-geosciences.wustl.edu/msl/msl-m-chemin-4-rdr-v1/mslcmn_1xxx/data/rdr4/cmb_587626717rda21420721316ch00111p1.csv, the Highfield 1D diffraction pattern can be found here: https://pds-geosciences.wustl.edu/msl/msl-m-chemin-4-rdr-v1/mslcmn_1xxx/data/rdr4/cma_595174954rda22270730550ch00111p1.csv, the Rock Hall 1D diffraction pattern of the first four minor frames can be found here: https://pds-geosciences.wustl.edu/msl/msl-m-chemin-4-rdr-v1/mslcmn_1xxx/data/rdr4/cma_598547494rda22650731206ch00111p1.csv, and the Rock Hall 1D diffraction pattern from the last two nights of analysis when grain motion was poor can be found here: https://pds-geosciences.wustl.edu/msl/msl-m-chemin-4-rdr-v1/mslcmn_1xxx/data/rdr4/cma_599656708rda22770731206ch00113p1.csv. The CheMin ODR provides diffraction data, fluorescence data, grain motion data, crystallographic information files used in the Rietveld refinements, descriptions of the analysis, and mineral abundances for all drill samples. Within the ODR, Duluth data can be found here: https://odr.io/CheMin#/view/288511/84/eyJkdF9pZCI6IjQzIn0/1, Stoer data can be found here: https://odr.io/CheMin#/view/288516/84/eyJkdF9pZCI6IjQzIn0/1, Highfield data can be found here: https://odr.io/CheMin#/view/288517/84/eyJkdF9pZCI6IjQzIn0/1, and Rock Hall data can be found here: https://odr.io/CheMin#/view/288518/84/eyJkdF9pZCI6IjQzIn0/1. A portion of this research was carried out at the Jet Propulsion Laboratory, California Institute of Technology, under a contract with the National Aeronautics and Space Administration.

## 7 References Cited

Achilles, C. N., Rampe, E. B., Downs, R. T., Bristow, T. F., Ming, D. W., Morris, R. V., Vaniman, D. T., Blake, D. F., Yen, A. S., McAdam, A. C., Sutter, B., Fedo, C. M., Gwizd, S., Thompson, L. M., Gellert, R., Morrison, S. M., Treiman, A. H., Chipera, S. J., Hazen, R. M., Craig, P. I., Des Marais, D. J., Grotzinger, J. P., Crisp, J. A., Tu, V. M., Castle, N., Downs, G. W., Peretyazhko, T. S., Walroth, R. C., and Thorpe, M. T. (submitted). Mineralogy of ancient fluvial-lacustrine sediments in Gale crater, Mars: Evidence for multiple diagenetic episodes. *Journal of Geophysical Research: Planets*.

Alpers, C. N., Rye, R. O., Nordstrom, D. K., White, L. D., and King, B.- S. (1992). Chemical, crystallographic and stable isotopic properties of alunite and jarosite from acid-Hypersaline Australian lakes. *Chemical Geology*, *96*(1-2), 203-226, http://dx.doi.org/10.1016/0009-2541(92)90129-S.

Altaner, S. P., and Grim, R. E. (1990). Mineralogy, chemistry, and diagenesis of tuffs in the Sucker Creek formation (Miocene), eastern Oregon. *Clays and Clay Minerals*, *38*(6), 561-572, http://dx.doi.org/10.1346/CCMN.1990.0380601.

Badaut, D., Decarreau, A., and Besson, G. (1992). Ferripyrophyllite and related Fe3+-rich 2:1 clays in recent deposits of Atlantis II Deep, Red Sea. *Clay Minerals*, *27*, 227-244.

Baker, L. L., and Neill, O. K. (2017). Geochemistry and mineralogy of a saprolite developed on Columbia River Basalt: Secondary clay formation, element leaching, and mass balance during weathering. *American Mineralogist*, *102*(8), 1632-1645, http://dx.doi.org/10.2138/am-2017-5964.

Banerdt, W. B., Smrekar, S. E., Banfield, D., Giardini, D., Golombek, M., Johnson, C. L., Lognonné, P., Spiga, A., Spohn, T., Perrin, C., Stähler, S. C., Antonangeli, D., Asmar, S., Beghein, C., Bowles, N., Bozdag, E., Chi, P., Christensen, U., Clinton, J., Collins, G. S., Daubar, I., Dehant, V., Drilleau, M., Fillingim, M., Folkner, W., Garcia, R. F., Garvin, J., Grant, J., Grott, M., Grygorczuk, J., Hudson, T., Irving, J. C. E., Kargl, G., Kawamura, T., Kedar, S., King, S., Knapmeyer-Endrun, B., Knapmeyer, M., Lemmon, M., Lorenz, R., Maki, J. N., Margerin, L., McLennan, S. M., Michaut, C., Mimoun, D., Mittelholz, A., Mocquet, A., Morgan, P., Mueller, N. T., Murdoch, N., Nagihara, S., Newman, C., Nimmo, F., Panning, M., Pike, W. T., Plesa, A.-C., Rodriguez, S., Rodriguez-Manfredi, J. A., Russel, C. T., Schmerr, N., Siegler, M., Stanley, S., Stutzmann, E., Teanby, N., Tromp, J., van Driel, M., Warner, N., Weber, R., Wieczorek, M. (2020). Initial results from the InSight mission on Mars. *Nature Geoscience*, *13*, 183-189, http://dx.doi.org/10.1038/s41561-020-544-y.

Banham, S. G., Gupta, S., Rubin, D. M., Watkins, J. A., Sumner, D. Y., Edgett, K. S., Grotzinger, J. P., Lewis, K. W., Edgar, L. A., Stack-Morgan, K. M., Barnes, R., Bell, J. F., III, Day, M. D., Ewing, R. C., Lapotre, M. G. A., Stein, N. T., Rivera-Hernandez, F., and Vasavada, A. R. (2018). Ancient Martian aeolian processes and palaeomorphology reconstructed from the Stimson formation on the lower slope of Aeolis Mons, Gale crater, Mars. *Sedimentology*, *65*(4), 993-1042, http://dx.doi.org/10.1111/sed.12469.

Barrón, V., Torrent, J., and Greenwood, J. P. (2006). Transformation of jarosite to hematite in simulated Martian brines. *Earth and Planetary Science Letters*, *251*(3-4), 380-385, http://dx.doi.org/10.1016/j.epsl.2006.09.022.

Bedford, C. C., Bridges, J. C., Schwenzer, S. P., Wiens, R. C., Rampe, E. B., Frydenvang, J., Gasda, P. J. (2019). Alteration trends and geochemical source region characteristics preserved in the fluviolacustrine sedimentary record of Gale crater, Mars. Geochim. Cosmochim. Acta 246, 234-266.

Berger, J. A., Schmidt, M. E., Gellert, R., Boyd, N. I., Desouza, E. D., Flemming, R. L., Izawa, M. R. M., Ming, D. W., Perrett, G. M., Rampe, E. B., Thompson, L. M., VanBommel, S. J. V., and Yen, A. S. (2017). Zinc and germanium in the sedimentary rocks of Gale Crater on Mars indicate hydrothermal enrichment followed by diagenetic fractionation. *Journal of Geophysical Research: Planets*, *122*(8), 1747-1772, http://dx.doi.org/10.1002/2017JE005290.

Bergmann, J. (2005). Rietveld Analysis Program BGMN. http://bgmn.de/BGMN_manual_2005.pdf.

Bibi, I., Singh, B., and Silvester, E. (2011). Akaganeite (b-FeOOH) precipication in inland acid sulfate soils of south-western New South Wales (NSW), Australia. *Geochimica et Cosmochimica Acta*, *75*, 6429-6438, https://doi.org/10.1016/j.gca.2011.08.019.

Blake, D., Vaniman, D., Achilles, C., Anderson, R., Bish, D., Bristow, T., Chen, C., Chipera, S., Crisp, J., Des Marais, D., Downs, R.T., Farmer, J., Feldman, S., Fonda, M., Gailhanou, M., Ma, H., Ming, D.W., Morris, R.V., Sarrazin, P., Stolper, E., Treiman, A., and Yen, A. (2012). Characterization and calibration of the CheMin mineralogical instrument on Mars Science Laboratory. *Space Science Reviews*, *170*(1-4), 341-399, http://dx.doi.org/10.1007/s11214-012-9905-1.

Blake, R. L., Hessevick, R. E., Zoltai, T., Finger, L. W. (1966). Refinement of the hematite structure. *American Mineralogist*, *51*, 123-129.

Bibring, J.-P., Langevin, Y., Mustard, J. F., Poulet, F., Arvidson, R., Gendrin, A., Gondet, B., Mangold, N., Pinet, P., Forget, F., the OMEGA team, Berthé, M., Gomez, C., Jouglet, D., Soufflot, A., Vincendon, M., Combes, M., Drossart, P., Encrenaz, T., Fouchet, T., Merchiorri, R., Belluci, G., Altieri, F., Formisano, V., Capaccioni, F., Cerroni, P., Coradini, A., Fonti, S., Korablev, Kottosov, V., Ignatiev, N., Moroz, V., Titov, D., Zasova, L., Loiseau, D., Doute, S., Schmitt, B., Sotin, C., Hauber, E., Hoffmann, H., Jaumann, R., Keller, U., Arvidson, R., Duxbury, T., and Neukum, G. (2006). Global mineralogical and aqueous Mars history derived from OMEGA/Mars Express data. *Science*, *312*(5772), 400-404.

Borlina, C. S., Ehlmann, B. L., and Kite, E. S. (2015). Modeling the thermal and physical evolution of Mount Sharp's sedimentary rocks, Gale crater, Mars: Implications for diagenesis on the MSL Curiosity rover traverse. *Journal of Geophysical Research: Planets*, *120*, 1396-1414, http://dx.doi.org/10.1002/2015JE004799.

Botz, R., and Bohrmann, G. (1991). Low-temperature opal-CT precipitation in Antarctic deep-sea sediments: evidence from oxygen isotopes. *Earth and Planetary Science Letters*, *107*(3-4), 612-617, http://dx.doi.org/10.1016/0012-821X(91)90105-Q.

Boynton, W. V., Taylor, G. J., Evans, L. G., Reedy, R. C., Starr, R., Janes, D. M., Kerry, K. E., Drake, D. M., Kim, K. J., Williams, R. M. S., Crombie, M. K., Dohm, J. M., Baker, V., Metzger, A. E., Karunatillake, S., Keller, J. M., Newsom, H. E., Arnold, J. R., Brückner, J., Englert, P. A. J., Gasnault, O., Sprague, A. L., Mitrofanov, I., Squyres, S. W., Trombka, J. I., d'Uston, L.,

Wänke, H., Hamara, D. K. (2007). Concentration of H, Si, Cl, K, Fe, and Th in the low-and mid-latitude regions of Mars. *Journal of Geophysical Research: Planets*, *112*(E12).

Bristow, T. F., Bish, D. L., Vaniman, D. T., Morris, R. V., Blake, D. F., Grotzinger, J. P., Rampe, E. B., Crisp, J. A., Achilles, C. N., Ming, D. W., Ehlmann, B. L., King, P. L., Bridges, J. C., Eigenbrode, J. L., Sumner, D. Y., Chipera, S. J., Morookian, J. M., Treiman, A. H., Morrison, S. M., Downs, R. T., Farmer, J. D., Des Marais, D., Sarrazin, P., Floyd, M. M., Mischna, M. A., McAdam, A. C. (2015). The origin and implications of clay minerals from Yellowknife Bay, Gale crater, Mars. *American Mineralogist*, *100*(4), 824-836.

Bristow, T. F., Rampe, E. B., Achilles, C. N., Blake, D. F., Chipera, S. J., Craig, P., Crisp, J. A., Des Marais, D. J., Downs, R. T., Gellert, R., Grotzinger, J. P., Gupta, S., Hazen, R. M., Horgan, B., Hogancamp, J. V., Mangold, N., Mahaffy, P. R., McAdam, A. C., Ming, D. W., Morookian, J. M., Morris, R. V., Morrison, S. M., Treiman, A. H., Vaniman, D. T., Vasavada, A. R., and Yen, A. S. (2018). Clay mineral diversity and abundance in sedimentary rocks of Gale crater, Mars. *Science Advances* (6), eaar3330.

Bristow, T. F., Rampe, E. B., Grotzinger, J. P., Fox, V. K., Bennett, K. A., Yen, A. S., Vasavada, A. R., Vaniman, D. T., Tu, V., Treiman, A. H., Thorpe, M. T., Morrison, S. M., Morris, R. V., Ming, D. W., McAdam, A. C., Malespin, C. A., Mahaffy, P. R., Hazen, R. M., Gupta, S., Downs, R. T., Downs, G. W., Des Marais, D. J., Crisp, J. A., Craig, P. I., Chipera, S. J., Castle, N., Blake, D. F., and Achilles, C. N. (2019). Clay minerals of Glen Torridon, Mount Sharp, Gale Crater. 9th International Conference on Mars, Abstract #6390.

Bryk, A. B., Dietrich, W. E., Lamb, M. P., Grotzinger, J. P., Vasavada, A. R., Stack, K. M., Arvidson, R., Fedo, C., Bennett, K., Fox, V. K., Gupta, S., Wiens, R. C., and Williams, R. M. E. (2019). In Curiosity's path; The geomorphology and stratigraphy of the Greenheugh pediment and Gediz Vallis ridge in Gale crater. In: Lunar and Planetary Science Conference (Vol. 50).

Buchwald, V. F., and Clarke, R. S. (1989). Corrosion of Fe-Ni alloys by Cl-containing akaganeite (β-FeOOH); the Antarctic meteorite case. *American Mineralogist*, *74*(5-6), 656-667.

Buick, R., and Dunlop, J. S. R. (1990). Evaporitic sediments of Early Archaean age from the Warrawoona Group, North Pole, Western Australia. *Sedimentology*, *37*(2), 247-277, http://dx.doi.org/10.1111/j.1365-3091.1990.tb00958.

Campbell, J. L., Perrett, G. M., Gellert, R., Andrushenko, S. M., Boyd, N. I., Maxwell, J. A., King, P. L., and Schofield, C. D. M., (2012). Calibration of the Mars Science Laboratory alpha particle X-ray spectrometer. *Space Science Reviews*, *170*(1-4), 319-340, http://dx.doi.org/10.1007/s11214-012-9873-5.

Catling, D. C., and Moore, J. M. (2003). The nature of coarse-grained crystalline hematite and its implications for the early environment of Mars. *Icarus*, *165*(2), 277-300, http://dx.doi.org/10.1016/S0019-1035(03)00173-8.

Carter, J., Viviano-Beck, C., Loizeau, D., Bishop, J., and Le Deit, L. (2015). Orbital detection and implications of akaganeite on Mars. *Icarus*, *253*, 296-310, http://dx.doi.org/10.1016/j.icarus.2015.01.020.

Chemtob, S. M., Nickerson, R. D., Morris, R. V., Agresti, D. G., and Catalano, J. G. (2017). Oxidative alteration of ferrous smectites and implications for the redox evolution of early Mars. *Journal of Geophysical Research: Planets*, *122*, 2469-2488, http://dx.doi.org/10.1002/2017JE005331.

Chi, G., Chu, H., Scott, R., Li, Z. (2015, August). Basin-scale hydrodynamic and fluid PTX characterization of the Athabasca Basin (Canada) and significance for unconformity-related U mineralization. In *The 13th SGA meeting* (pp. 1793-1796).

Chipera, S. J., and Bish, D. L. (2002). FULLPAT: a full-pattern quantitative analysis program for X-ray powder diffraction using measured and calculated patterns. *Journal of Applied Crystallography*, *35*(6), 744-749, http://dx.doi.org/10.1107/S0021889802017405.

Chipera, S. J., and Bish, D. L. (2013). Fitting full X-ray diffraction patterns for quantitative analysis: a method for readily quantifying crystalline and disordered phases. *Advances in Materials Physics and Chemistry*, *3*(01), 47-53, http://dx.doi.org/10.4236/ampc.2013.31.A007.

Christensen, P. R., Bandfield, J. L., Clark, R. N., Edgett, K. S., Hamilton, V. E., Hoefen, T., Kieffer, H. H., Kuzmin, R. O., Lane, M. D., Malin, M. C., Morris, R. V., Pearl, J. C., Pearson, R., Roush, T. L., Ruff, S. W., and Smith, M. D. (2000). Detection of crystalline hematite mineralization on Mars by the Thermal Emission Spectrometer: Evidence for near-surface water. *Journal of Geophysical Research: Planets*, *105*(E4), 9623-9642, http://dx.doi.org/10.1029/1999JE001093.

Cornell, R. M., and Giovanoli, R. (1990). Transformation of akaganeite into goethite and hematite in alkaline media. *Clays and Clay Minerals*, *38*(5), 469-476, https://doi.org/10.1346/CCMN.1990.0380502.

Craig, P. I., Ming, D. W., and Rampe, E. B. (2014). Sulfate formation from acid-weathered phyllosilicates: Implications for the aqueous history of Mars. Eighth International Conference on Mars. Abstract 1323.

Cruft, E. F., and Chao, P. C. (1970). Nucleation kinetics of the gypsum-anhydrite system. In: 3rd symposium on salt, northern Ohio geological society proceedings, vol. 1, pp. 109-118.

Cuadros, J., Michalski, J. R., Dekov, V., Bishop, J., Fiore, S., Dyar, M. D. (2013). Crystal-chemistry of interstratified Mg/Fe-clay minerals from seafloor hydrothermal sites. *Chemical Geology*, *360-361*, 142-158, http://dx.doi.org/10.1016/j.chemgeo.2013.10.1016.

Dang, M.-Z., Rancourt, D. G., Dutrizac, J. E., Lamarche, G., Provencher, R. (1998). Interplay of surface conditions, particle size, stoichiometry, cell parameters, and magnetism in synthetic

hematite-like materials. *Hyperfine Interactions*, *117*, 271-319, http://dx.doi.org/10.1023/A:1012655729417.

David, G., Cousin, A., Forni, O., Meslin, P.-Y., Dehouck, E., Mangold, N., L'Haridon, J., Rapin, W., Gasnault, O., Johnson, J. R., Ollila, A. M., Newell, A. R., Fraeman, A. A., Wiens, R. C., Maurice, S., Salvatore, M., and Frydenvang, J. (this issue). Iron oxide mineral grains observed by ChemCam across Vera Rubin ridge sedimentary rocks at Gale crater, Mars. *Journal of Geophysical Research: Planets*.

Decarreau, A., Petit, S., Martin, F., Farges, F., Vieillard, P., and Joussein, E. (2008). Hydrothermal synthesis, between 70 and 150 °C, of high-charge, ferric nontronites. *Clays and Clay Minerals*, *56*(3), 322-337, http://dx.doi.org/10.1346/CCMN.2008.0560303.

Deliyanni, E. A., Bakoyannakis, D. N., Zouboulis, A. I., Matis, K. A., and Nalbandian, L. (2001). Akaganeite-type β-FeO(OH) nanocrystals: preparation and characterization. *Microporous and Mesoporous Materials*, *42*, 49-57.

Dixon, E. M., Elwood Madden, A. S., Hausrath, E. M., and Elwood Madden, M. E. (2015). Assessing hydrodynamic effects on jarosite dissolution rates, reaction products, and preservation on Mars. *Journal of Geophysical Research: Planets*, *120*(4), 625-642.

Dera, P., Zhuravlev, K., Prakapenka, V., Rivers, M. L., Finkelstein, G. J., Grubor-Urosevic, O., Tschauner, O., Clark, S. M., and Downs, R. T. (2013). High pressure single-crystal micro X-ray diffraction analysis with GSE_ADA/RSV software. *High Pressure Research*, *33*(3), 466-484, http://dx.doi.org/10.1080/08957959.2013.806504.

Driscoll, R. L., and Leinz, R. W. (2005). Methods for synthesis of some jarosites. U.S. Geological Survey Techniques and Methods 5-D1, p. 5.

Edgar, L. A., Fedo, C. M., Gupta, S., Banham, S. G., Fraeman, A. A., Grotzinger, J. P., Stack, K. M., Stein, N. T., Bennett, K. A., Rivera-Hernandez, F., Sun, V. Z., Edgett, K. S., Rubin, D. M., House, C., Van Beek, J. (2020, *this issue*). A lacustrine paleoenvironment recorded at Vera Rubin ridge, Gale crater: Overview of the sedimentology and stratigraphy observed by the Mars Science Laboratory Curiosity rover. *Journal of Geophysical Research: Planets*, *125*(3), http://dx.doi.org/10.1029/2019JE006307.

Egenhoff, S. O., Fishman, N. S., Lowers, H. A., Ahlberg, P. (2019). The complexity of mudstone diagenesis–some insight from the Tøyen Shale, Lower to Middle Ordovician, southern Sweden. *GFF*, *141*(1), 54-67.

Egglseder, M. S., Cruden, A. R., Tomkins, A. G., Wilson, S. A., Dalstra, H. J., Rielli, A., Li, C., Baumgartner, J., and Faivre, D. (2019). Tiny particles building huge ore deposits – Particle-based crystallization in banded iron formation-hosted iron ore deposits (Hamersley Province, Australia. *Ore Geology Reviews*, *104*, 160-174, http://dx.doi.org/10.1016/j.oregeorev.2018.10.001.

Ehlmann, B. L., and Edwards, C. S. (2014). Mineralogy of the martian surface. *Annual Reviews of Earth and Planetary Sciences*, *42*, 291-315, http://dx.doi.org/10.1146/annurevearth-060313-055024.

Elmore, R. D., Heij, G. W., Wickard, A. K. (2016). Paragenesis of mineralized fractures and diagenesis of prominent North American shales. *The Sedimentary Record: SEPM*, *14*, 4-10, http://dx.doi.org/10.2110/sedred.2016.4.

Elwood Madden, M. E., Madden, A. S., Rimstidt, J. D., Zahrai, S., Kendall, M. R., and Miller, M. A. (2012). Jarosite dissolution rates and nanoscale mineralogy. *Geochimica et Cosmochimica Acta*, *91*, 306-321, http://dx.doi.org/10.1016/j.gca.2012.05.001.

España, J. S., Pamo, E. L., Santofimia, E., Aduvire, O., Reyes, J., and Barettino, D. (2005). Acid mine drainage in the Iberian Pyrite Belt (Odiel river watershed, Huelva, SW Spain): Geochemistry, mineralogy and environmental implications. *Applied Geochemistry*, *20*(7), 1320-1356, http://dx.doi.org/10.1016/j.apgeochem.2005.01.011.

Fontes, M. P. F., and Weed, S. B. (1991). Iron oxides in selected Brazilian oxisols: I. Mineralogy. *Soil Science Society of America Journal*, *55*(4), 1143-1149, http://dx.doi.org/10.2136/sssaj1991.03615995005500040040x.

Fraeman, A. A., Arvidson, R. E., Catalano, J. G., Grotzinger, J. P., Morris, R. V., Murchie, S. L., Stack, K. M., Humm, D. C., McGovern, J. A., Seelos, F. P., Seelos, K. D., and Viviano, C. E. (2013). A hematite-bearing layer in Gale Crater, Mars: Mapping and implications for past aqueous conditions. *Geology*, *41*(10), 1103-1106, http://dx.doi.org/10.1130/G34613.1.

Fraeman, A. A., Ehlmann, B. L., Arvidson, R. E., Edwards, C. S., Grotzinger, J. P., Milliken, R. E., Quinn, D. P., and Rice, M. S. (2016). The stratigraphy and evolution of lower Mount Sharp from spectral, morphological, and thermophysical data sets. *Journal of Geophysical Research: Planets*, *121*, 1713-1736, http://dx.doi.org/10.1002/2016JE005095.

Fraeman, A. A., Catalano, J. G., Edgar, L., Fedo, C., Rampe, E., Morris, R. V., Vasavada, A. R., Sun, V. Z., Arvidson, R. E., Bryk, A., Banham, S., Bennett, K., Bridges, J. C., Dietrich, W., Edwards, C. S., Fischer, W. W., Fox, V., Frydenvang, J., Hardgrove, C., Grotzinger, J. P., Gupta, S., Horgan, B., House, C., Johnson, S., Jacob, S., Johnson, J., L'Haridon, J., Mangold, N., Rubin, D., Salvatore, M., Schwenzer, S. P., Siebach, K., Stein, N. T., Stack, K. M., Thompson, L. M., Wellington, D., Williams, A., Turner, S. (*this issue*). The origin of Vera Rubin ridge: Overview and results from *Curiosity's* exploration campaign. *Journal of Geophysical Research: Planets*.

Fu, X., Jia, L., Wang, A., Cao, H., Ling, Z., Liu, C., Shi, E., Wu, Z., Li, B., Zhang, J. (2020). Thermal stability of akaganeite and its desiccation process under conditions relevant to Mars. *Icarus*, *336*, http://dx.doi.org/10.1016/j.icarus.2019.113435.

Glotch, T. D., and Kraft, M. D. (2008). Thermal transformations of akaganeite and lepidocrocite to hematite: assessment of possible precursors to martian crystalline hematite. *Physics and Chemistry of Minerals*, *35*(10), 596-581, http://dx.doi.org/10.1007/s00269-008-0249-z.

Golden, D. C., Ming, D. W., Morris, R. V., and Graff, T. G. (2008). Hydrothermal synthesis of hematite spherules and jarosite: Implications for diagenesis and hematite spherule formation in sulfate outcrops at Meridiani Planum, Mars, *American Mineralogist*, *93*, 1201-1214, http://dx.doi.org/10.2138/am.2008.2737.

Golombek, M., Grant, J., Kipp, D., Vasavada, A., Kirk, R., Fergason, R., Belluta, P., Calef, F., Larsen, K., Katayama, Y., Huertas, A., Beyer, R., Chen, A., Parker, T., Pollard, B., Lee, S., Sun, Y., Hoover, R., Sladek, H., Grotzinger, J., Welch, R., Noe Dobrea, E., Michalski, J., and Watkins, M. (2012). Selection of the Mars Science Laboratory landing site. *Space Science Reviews*, *170*, 641-737, http://dx.doi.org/10.1007/s11214-012-9916-y.

Grotzinger, J. P., Sumner, D. Y., Kah, L. C., Stack, K., Gupta, S., Edgar, L., Rubin, D., Lewis, K., Schieber, J., Mangold, N., Milliken, R. Conrad, P. G., Des Marais, D., Farmer, J., Siebach, K., Calef III, F., Hurowitz, J., McLennan, S. M., Ming, D., Vaniman, D., Crisp, J., Vasavada, A., Edgett, K. S., Malin, M., Blake, D., Gellert, R., Mahaffy, P., Wiens, R. C., Maurice, S., Grant, J. A., Wilson, S., Anderson, R. C., Beegle, L., Arvidson, R., Hallet, B., Sletten, R. S., Rice, M., Bell III, J., Griffes, J., Ehlmann, B., Anderson, R. B., Bristow, T. F., Dietrich, W. E., Dromart, G., Eigenbrode, J., Fraeman, A., Hardgrove, C., Herkenhoff, K., Jandura, L., Kocurek, G., Lee, S., Leshin, L. A., Leveille, R., Limonadi, D., Maki, J., McCloskey, S., Meyer, M., Minitti, M., Newsom, H., Oehler, D., Okon, A., Palucis, M., Parker, T., Rowland, S., Schmidt, M., Squyres, S., Steele, A., Stolper, E., Summons, R., Treiman, A., Williams, R., Yingst, A., MSL Science Team (2014). A habitable fluvio-lacustrine environment at Yellowknife Bay, Gale Crater, Mars. *Science*, 343(6169), http://dx.doi.org/10.1126/science.1242777.

Grotzinger, J. P., Gupta, S., Malin, M. C., Rubin, D. M., Schieber, J., Siebach, K., Sumner, D. Y., Stack, K. M., Vasavada, A. R., Arvidson, R. E., Calef III, F., Edgar, L., Fischer, W. F., Grant, J. A., Griffes, J., Kah, L. C., Lamb, M. P., Lewis, K. W., Mangold, N., Minitti, M. E., Palucis, M., Rice, M., Williams, R. M. E., Yingst, R. A., Blake, D., Blaney, D., Conrad, P., Crisp, J., Dietrich, W. E., Dromart, G., Edgett, K. S., Ewing, R. C., Gellert, R., Hurowitz, J. A., Kocurek, G., Mahaffy, P., McBride, M. J., McLennan, S. M., Mischna, M., Ming, D., Milliken, R., Newsom, H., Oehler, D., Parker, T. J., Vaniman, D., Wiens, R. C., Wilson, S. A., (2015). Deposition, exhumation, and paleoclimate of an ancient lake deposit, Gale crater, Mars. *Science*, *350*(6257), aac7575, http://dx.doi.org/10.1126/science.aac7575.

Gulick, V. C. (1998). Magmatic intrusions and a hydrothermal origin for fluvial valleys on Mars. *Journal of Geophysical Research*, *103*(E8), 19,365-19,387.

Guo, H., and Barnard, A. S. (2011). Thermodynamic modelling of nanomorphologies of hematite and goethite. *Journal of Materials Chemistry*, *21*, 11566, http://dx.doi.org/10.1039/c1jm10381d.

Guo, H., and Barnard, A. S. (2013). Naturally occurring iron oxide nanoparticles: morphology, surface chemistry and environmental stability. *Journal of Materials Chemistry A*, *1*(1), 27-42, http://dx.doi.org/10.1039/C2TA00523A.

Hahn, B. C., McLennan, S. M., Klein, E. C. (2011). Martian surface heat production and crustal heat flow from Mars Odyssey Gamma-Ray spectrometry. *Geophysical Research Letters*, *38*(14).

Harper, D. A., Longstaffe, F. J., Wadleigh, M. A., McNutt, R. H. (1995). Secondary K-feldspar at the Precambrian–Paleozoic unconformity, southwestern Ontario. *Canadian Journal of Earth Sciences*, *32*(9), 1432-1450.

Hausrath, E. M., Ming, D. W., Peretyazhko, T. S., and Rampe, E. B. (2018). Reactive transport and mass balance modeling of the Stimson sedimentary formation and altered fracture zones constrain diagenetic conditions at Gale crater, Mars. *Earth and Planetary Science Letters*, *491*, 1-10, http://dx.doi.org/10.1016/j.epsl.2018.02.037.

Hannington, M., Herzig, P., Stoffers, P., Scholten, J., Botz, R., Garbe-Schönberg, D., Jonasson, I. R., Roest, W., and Shipboard Scientific Party (2001). First observations of high-temperature submarine hydrothermal vents and massive anhydrite deposits off the north coast of Iceland. *Marine Geology*, *177*(3-4), 199-220, http://dx.doi.org/10.1016/S0025-3227(01)00172-4.

Harder, H. (1976). Nontronite synthesis at low temperatures. *Chemical Geology*, *18*, 169-180.

Hardie, L. A. (1967). The gypsum-anhydrite equilibrium at one atmosphere pressure. *American Mineralogist*, *52*, 171–200.

Holm, N. G., Dowler, M. J., Wadsten, T., and Arrhenius, G. (1983). β-FeOOH•$Cl_n$ (akaganeite) and $Fe_{1-x}O$ (wüstite) in hot brine from the Atlantic II Deep (Red Sea) and the uptake of amino acids by β-FeOOH•$Cl_n$. *Geochimica et Cosmochimica Acta*, *47*(8), 1465-1470, http://dx.doi.org/10.1016/0016-7037(83)90305-8.

Holtstam, D. (2006) Akaganeite as a corrosion product of natural, non-meteoritic iron from Qeqertarsuaq, West Greenland. *GFF*, *128*(1), 69-71, http://dx.doi.org/10.1080/11035890601281069.

Horgan, B., Johnson, J. R., Fraeman, A. A., Rice, M. S., Seeger, C., Bell III, J. F., Bennett, K. A., Cloutis, E. A., Frydenvang, J., L'Haridon, J., Mangold, N., Edgar, L. A., Grotzinger, J. P., Jacob, S. R., Rampe, E. B., Rivera-Hernandez, F., Sun, V. Z., Thompson, L. M., Wellington, D. (*this issue*). *Journal of Geophysical Research: Planets*.

Iler, R. K. (1979). The Chemistry of Silica: Solubility, polymerization, colloid and surface properties, and biochemistry. Wiley, New York.

Iyer, K., Rüpke, L., Galerne, C. Y. (2013). Modeling fluid flow in sedimentary basins with sill intrusions: Implications for hydrothermal venting and climate change. *Geochemistry, Geophysics, Geosystems*, *14*(12), http://dx.doi.org/10.1002/2013GC005012.

Jacob, S. R., Wellington, D. F., Bell III, J. F., Achilles, C., Fraeman, A. A., Horgan, B., Johnson, J. R., Peters, G. H., Rampe, E. B., and Thompson, L. M. (*this issue*). Spectral, compositional,

and physical properties of the upper Murray formation and Vera Rubin ridge, Gale crater, Mars. *Journal of Geophysical Research: Planets*.

Johnston, J. H. (1977). Jarosite and akaganeite from White Island volcano, New Zealand: An X-ray and Mossbauer study. *Geochimica et Cosmochimica Acta*, *41*(4), 539-544, http://dx.doi.org/10.1016/0016-7037(77)90291-5.

Kastner, M., Keene, J. B., and Gieskes, J. M. (1977). Diagenesis of siliceous oozes – I. Chemical controls on the rate of opal-A to opal-CT transformation – an experimental study. *Geochimica et Cosmochimica Acta*, *41*(8), 1041-1051, http://dx.doi.org/10.1016/0016-7037(77)9099-0.

Keeling, J. L., Raven, M. D., and Gates, W. P. (2000). Geology and characterization of two hydrothermal nontronites from weathered metamorphic rocks at the Uley Graphite Mine, South Australia. *Clays and Clay Minerals*, *48*(5), 537-548, http://doi.org/10.1346/CCMN.2000.0480506.

Kloprogge, J. T., Komarneni, S., and Amonette, J. E. (1999). Synthesis of smectite clay minerals: A critical review. *Clays and Clay Minerals*, *47*(5), 529-554, http://doi.org/10.1346/CCMN.1999.0470501.

Komadel, P., Hrobáriková, J., Smrcok, L., and Koppelhuber-Bitschnau, B. (2002). Hydration of reduced-charge montmorillonite. *Clay Minerals*, *37*(3), 543-550, http://dx.doi.org/10.1180/0009855023730057.

Kronyak, R. E., Kah, L. C., Edgett, K. S., VanBommel, S. J., Thompson, L. M., Wiens, R. C., Sun, V. Z., and Nachon, M. (2019). Mineral-filled fractures as indicators of multigenerational fluid flow in the Pahrump Hills member of the Murray formation, Gale crater, Mars. *Earth and Space Science*, *6*(2), 238-265, http://dx.doi.org/10.1029/2018EA000482.

Kunda, W., and Veltman, H. (1979). Decomposition of jarosite. *Metallurgical Transactions B*, *10*(3), 439-446, http://dx.doi.org/10.1007/BF02652517.

L'Haridon, J., Mangold, N.; Meslin, P.-Y., Johnson, J. R., Rapin, W., Forni, O., Cousin, A., Payré, V., Dehouck, E., Nachon, M., Le Deit, L., Gasnault, O., Maurice, S., Wiens, R. (2018). Chemical variability in mineralized veins observed by ChemCam on the lower slopes of Mount Sharp in Gale crater, Mars. *Icarus*, *311*, 69-86, http://dx.doi.org/10.1016/j.icarus.2018.01.028

L'Haridon, J., Mangold, N., Fraeman, A. A., Johnson, J. R., Cousin, A., Rapin, W., David, G., Dehouck, E., Sun, V., Frydenvang, J., Gasnault, O., Gasda, P., Lanza, N., Forni, O., Meslin, P. -Y., Schwenzer, S., Bridges, J., Horgan, B., House, C., Salvatore, M., Maurice, S., and Wiens, R. C. (*this issue*) Iron mobility during diagenesis as observed by ChemCam at the Vera Rubin ridge, Gale crater, Mars. *Journal of Geophysical Research: Planets*.

Lane, M. D., Morris, R. V., Mertzman, S. A., and Christensen, P. R. (2002). Evidence for platy hematite grains in Sinus Meridiani, Mars. *Journal of Geophysical Research: Planets*, *107*(E12), http://dx.doi.org/10.1029/2001JE001832.

Lasaga, A. C. (1984). Chemical kinetics of water-rock interactions. *Journal of Geophysical Research: Solid Earth*, *89*(B6), 4009-4025, http://dx.doi.org/10.1029/JB089iB06p04009.

Laverret, E., Mas, P. P., Beaufort, D., Kister, P., Quirt, D., Bruneton, P., Clauer, N. (2006). Mineralogy and geochemistry of the host-rock alterations associated with the Shea Creek unconformity-type uranium deposits (Athabasca Basin, Saskatchewan, Canada). Part 1. Spatial variation of illite properties. *Clays and Clay Minerals*, *54*(3), 275-294.

Le Deit, L., Mangold, N., Forni, O., Cousin, A., Lasue, J., Schröder, S., Wiens, R.C., Sumner, D., Fabre, C., Stack, K.M, Anderson, R.B., Blaney, D., Clegg, S., Dromart, G., Fisk, M., Gasnault, O., Grotzinger, J.P., Gupta, S., Lanza, N., Le Mouélic, S., Maurice, S., McLennan, S.M., Meslin, P.-Y., Nachon, M., Newsom, H., Payré, V., Rapin, W., Rice, M., Sautter, V., Treiman, A.H. (2016). The potassic sedimentary rocks in Gale Crater, Mars, as seen by ChemCam on board Curiosity. *Journal of Geophysical Research – Planets*, *121*(5), 784-804.

Lognonné, P., Banerdt, W. B., Pike, W. T., Giardini, D., Christensen, U., Garcia, R. F., Kawamura, T., Kedar, S., Knapmeyer-Endrun, B., Margerin, L., Nimmo, F., Panning, M., Tauzin, B., Scholz, J.-R., Antonanglei, D., Barkaoui, S., Beucler, E., Bissig, F., Brinkman, N., Calvet, M., Ceylan, S., Charalambous, C., Davis, P., van Driel, M., Drilleau, M., Fayon, L., Joshi, R., Kenda, B., Khan, A., Knapmeyer, M., Lekic, V., McClean, J., Mimoun, D., Murdoch, N., Pan, L., Perrin, C., Pinot, B., Pou, L., Menina, S., Rodriguez, S., Schmelzbach, C., Schmerr, N., Sollberger, D., Spiga, A., Stähler, S., Stott, A., Stutzmann, E., Tharimena, S., Widmer-Schnidrig, R., Andersson, F., Ansan, V., Beghein, C., Böse, M., Bozdag, E., Clinton, J., Daubar, I., Delage, P., Fuji, N., Golombek, M., Grott, M., Horleston, A., Hurst, K., Irving, J., Jacob, A., Knollenberg, J., Krasner, S., Krause, C., Lorenz, R., michaut, C., Myhill, R., Nissen-Meyer, T., ten Pierick, J., Plesa, A-C., Quantin-Nataf, C., Robertsson, J., Rochas, L., Schimmel, M., Smrekar, S., Spohn, T., Teanby, N., Tromp, J., Vallade, J., Verdier, N., Vrettos, C., Weber, R., Banfield, D., Barrett, E., Bierwirth, M., Calcutt, S., Compaire, N., Johnson, C. L., Mance, D., Euchner, F., Kerjean, L., Mainsant, G., Mocquet, A., Rodriguez Manfredi, J. A., Pont, G., Laudet, P., Nebut, T., de Raucourt, S., Robert, O., Russell, C. T., Sylvestre-Baron, A., Tillier, S., Warren, T., Wieczorek, M., Yana, C., Zweifel, P. (2020). Constraints on the shallow elastic and anelastic structure of Mars from InSight seismic data. *Nature Geoscience*, *13*, 213-220, http://dx.doi.org/10.1038/s41561-020-0536.

Lynne, B. Y., and Campbell, K. A. (2004). Morphologic and mineralogic transitions from opal-A to opal-CT in low-temperature siliceous sinter diagenesis, Taupo Volcanic Zone, New Zealand. *Journal of Sedimentary Research*, *74*(4), 561-579.

Madden, A. S., Hamilton, V. E., Elwood Madden, M. E., Larson, P. R., and Miller, M. A. (2010). Low-temperature mechanism for formation of coarse crystalline hematite through nanoparticle aggregation. *Earth and Planetary Science Letters*, *298*(3-4), 377-384, http://dx.doi.org/10.1016/j.epsl.2010.08.014.

Mangold, N., E. Dehouck, C. Fedo, O. Forni, C. Achilles, T. Bristow, R. T. Downs, J. Frydenvang, O. Gasnault, J. L'Haridon, L. Le Deit, S. Maurice, S.M. McLennan, P.-Y. Meslin,

S. Morrison, H.E. Newsom, E. Rampe, W. Rapin, F. Rivera-Hernandez, M. Salvatore, R.C. Wiens (2019). Chemical alteration of fine-grained sedimentary rocks at Gale crater. *Icarus*, *321*, 619-631, http://dx.doi.org/10.1016/j.icarus.2018.11.004.

Martin, P. E., Farley, K. A., Baker, M. B., Malespin, C. A., Schwenzer, S. P., Cohen, B. A., Mahaffy, P. R., McAdam, A. C., Ming, D. W., Vasconcelos, P. M., and Navarro-González, R. (2017). A Two-Step K-Ar Experiment on Mars: Dating the Diagenetic Formation of Jarosite from Amazonian Groundwaters. *Journal of Geophysical Research: Planets*, *122*(12), 2803-2818, http://dx.doi.org/10.1002/2017JE005445.

McAdam, A. C., Sutter, B., Archer Jr., P. D., Franz, H. B., Wong, G. M., Lewis, J. M. T., Eigenbrode, J. L., Stern, J. C., Knudson, C. A., Clark, J. V., Andrejkovičová, S., Ming, D. W., Morris, R. V., Achilles, C. N., Rampe, E. B., Bristow, T. F., Navarro-González, R., Mahaffy, P. R., Thompson, L. M., Gellert, R., Williams, A. J., House, C. H., Johnson, S. S. (*this issue*). Constraints on the mineralogy and geochemistry of the Vera Rubin ridge, Gale crater, Mars, from Mars Science Laboratory Sample Analysis at Mars evolved gas analysis. *Journal of Geophysical Research: Planets*.

McLennan, S. M. (2003). Sedimentary silica on Mars. Geology, 31(4), 315-318, http://dx.doi.org/10.1130/0091-7613(2003)031<0315:SSOM>2.0.CO;2.

McLennan, S. M., Anderson, R. B., Bell III, J. F., Bridges, J. C., Calef, F., Campbell, J. L., Clark, B. C., Clegg, S., Conrad, P., Cousin, A., Des Marais, D. J., Dromart, G., Dyar, M. D., Edgar, L. A., Ehlmann, B. L., Fabre, C., Forni, O., Gasnault, O., Gellert, R., Gordon, S., Grant, J. A., Grotzinger, J. P., Gupta, S., Herkenhoff, K. E., Hurowitz, J. A., King, P. L., Le Mouélic, S., Leshin, L. A., Léveillé, R., Lewis, K. W., Mangold, N., Maurice, S., Ming, D. W., Morris, R. V., Nachon, M., Newsom, H. E., Ollila, A. M., Perrett, G. M., Rice, M. S., Schmidt, M. E., Schwenzer, S. P., Stack, K., Stolper, E. M., Sumner, D. Y., Treiman, A. H., VanBommel, S., Vaniman, D. T., Vasavada, A., Wiens, R. C. (2014). Elemental geochemistry of sedimentary rocks at Yellowknife Bay, Gale crater, Mars. *Science*, *343*(6169), 1244734.

Meunier, A. (2005). Clays. *Springer*, New York, 472 pp.

Meyer, C. (2003). Mars meteorite compendium, Lyndon B. Johnson Space Cent., NASA, Houston, Tex.

Michalski, J. R., Cuadros, J., Bishop, J. L., Dyar, M. D., Dekov, V., Fiore, S. (2015). Constraints on the crystal-chemistry of Fe/Mg-rich smectitic clays on Mars and links to global alteration trends. *Earth and Planetary Science Letters*, *427*, 215-225, http://dx.doi.org/10.1016/j.epsl.2015.06.020.

Miller, K. (2017). Anhydrite nucleation and growth at low temperatures: Effects of flow rate, activity of water, and mineral substrates. (MS Thesis, U of OK).

Miller, K. M., Phillips-Lander, C. M., Elwood Madden, A. S., and Elwood Madden, M. E. (2016, March). Low Temperature Anhydrite Formation in Flow-Through Dissolution Experiments. In Lunar and Planetary Science Conference (Vol. 47, p. 1308).

Milliken, R. E., Grotzinger, J. P., and Thomson, B. J. (2010). Paleoclimate of Mars as captured by the stratigraphic record in Gale Crater. *Geophysical Research Letters*, *37*(4), http://dx.doi.org/10.1029/2009GL041870.

Minitti, M. E., Lane, M. D., and Bishop, J. L. (2005). A new hematite formation mechanism for Mars. *Meteoritics and Planetary Science*, *40*(1), 55-69, http://dx.doi.org/10.1111/j.1945-5100.2005.tb00364.

Morris, R. V., Ming, D., Golden, D. C., Arvidson, R. E., Wiseman, S. M., Lichtenberg, K. A., Cull, S., Graff, T. G. (2009). Visible and near-IR reflectance spectra for smectite, sulfate and perchlorate under dry conditions for interpretation of martian surface mineralogy. In: Lunar and Planetary Science Conference (Vol. 40).

Morris, R. V., Golden, D. C., Bell III, J. F., Shelfer, T. D., Scheinost, A. C., Hinman, N. W., Furniss, G., Mertzman, S. A., Bishop, J. L., Ming, D. W., Allen, C. C., and Britt, D. T. (2000). Mineralogy, composition, and alteration of Mars Pathfinder rocks and soils: Evidence from multispectral, elemental, and magnetic data on terrestrial analogue, SNC meteorite, and Pathfinder samples. *Journal of Geophysical Research: Planets*, *105*(E1), 1757-1817, http://dx.doi.org/10.1029/1999JE001059.

Morris, R. V., Rampe, E. B., Graff, T. G., Archer Jr., P. D., Le, L., Ming, D. W., Sutter, B. (2015). Transmission X-ray diffraction (XRD) patterns relevant to the MSL CheMin amorphous component: Sulfates and silicates. In: Lunar and Planetary Science Conference (Vol. 46).

Morris, R. V., Vaniman, D. T., Blake, D. F., Gellert, R., Chipera, S. J., Rampe, E. B., Ming, D. W., Morrison, S. M., Downs, R. T., Treiman, A. H., Yen, A. S., Grotzinger, J. P., Achilles, C. N., Bristow, T. F., Crisp, J. A., Des Marais, D. J., Farmer, J. D., Fendrich, K. V., Frydenvang, J., Graff, T. G., Morookian, J. M., Stolper, E. M., and Schwenzer, S. P. (2016). Silicic volcanism on Mars evidenced by tridymite in high-$SiO_2$ sedimentary rock at Gale crater. *Proceedings of the National Academy of Sciences*, *113*(26), 7071-7076, http://dx.doi.org/10.1073/pnas.1607098113.

Morris, R. V., Rampe, E. B., Vaniman, D. T., Christoffersen, R., Yen, A. S., Morrison, S. M., Ming, D. W., Fraeman, A. A., Le, L., Tu, V. M., Ott, J. P., Hogancamp, J. V., Graff, T. G., Adams, M., Hamilton, J. C., Mertzman, S. A., Achilles, C. N., Bristow, T. F., Blake, D. F., Castle, N., Chipera, S. J., Craig, P. I., Crisp, J., Des Marais, D. J., Downs, G., Downs, R. T., Hazen, R. M., Morookian, J. M., Thorpe, M., Treiman, A. H. (*this issue*). Hydrothermal precipitation of sanidine (adularia) having extreme Al,Si structural disorder and specular hematite at Mauakea volcano (Hawaii) and at Gale crater (Mars). *Journal of Geophysical Research: Planets*.

Morrison, S. M., Downs, R. T., Blake, D. F., Prabhu, A. E., Vaniman, D. T., Ming, D. W., Rampe, E. B., Hazen, R. M., Achilles, C. N., Treiman, A. H., Yen, A. S., Morris, R. V., Bristow,

T. F., Chipera, S. J., Sarrazin, P. C., Fendrich, K. V., Morookian, J. M., Farmer, J. D., Des Marais, D. J., and Craig, P. I. (2018). Relationships between unit-cell parameters and composition for rock-forming minerals on Earth, Mars, and other extraterrestrial bodies. *American Mineralogist*, *103*(6), 848-856, http://dx.doi.org/10.2138/am-2018-6123.

Nachon, M., Clegg, S. M., Mangold, N., Schröder, S., Kah, L. C., Dromart, G., Ollila, A., Johnson, J. R., Oehler, D. Z., Bridges, J. C., Le Mouélic, S., Forni, O., Wiens, R. C., Anderson, R. B., Blaney, D. L., Bell III, J. F., Clark, B., Cousin, A., Dyar, M. D., Ehlmann, B., Fabre, C., Gasnault, O., Grotzinger, J., Lasue, J., Lewin, E., Léveillé, R., McLennan, S., Maurice, S., Meslin, P. -Y., Rapin, W., Rice, M., Squyres, S. W., Stack, K., Sumner, D. Y., Vaniman, D., and Wellington, D. (2014). Calcium sulfate veins characterized by ChemCam/Curiosity at Gale crater, Mars. *Journal of Geophysical Research: Planets*, *119*(9), 1991-2016, http://dx.doi.org/10.1002/2013JE004588.

Nordstrom, D. K. (1982). Aqueous pyrite oxidation and the consequent formation of secondary iron minerals. *Acid sulfate weathering*, *10*, 37-56.

Novák, I., and Číčel, B. (1978). Dissolution of smectites in hydrochloric acid: II. Dissolution rate as a function of crystallochemical composition. Clays and Clay Minerals, 26(5), 341-344, http://dx.doi.org/10.1346/CCMN.1978.

Ossorio, M., Van Driessche, A. E. S., Pérez, P., García-Ruiz, J. M. (2014). The gypsum-anhydrite paradox revisited. *Chemical Geology*, *386*, 16-21, http://dx.doi.org/10.1016/j.chemgeo.2014.07.026.

Ostroff, A. G. (1964). Conversion of gypsum to anhydrite in aqueous salt solutions. *Geochimica et Cosmochimica Acta*, *28*(9), 1363-1372, http://dx.doi.org/10.1016/0016-7037(64)90154-1.

Patterson, A. L. (1939). The Scherrer formula for X-ray particle size determination. *Physical review*, *56*(10), 978, http://dx.doi.org/10.1103/PhyRev.56.978.

Peretyazhko, T. S., Fox, A., Sutter, B., Niles, P. B., Adams, M., Morris, R. V., and Ming, D. W. (2016). Synthesis of akaganeite in the presence of sulfate: Implications for akaganeite formation in Yellowknife Bay, Gale crater, Mars. *Geochimica et Cosmochimica Acta*, *188*, 284-296, http://dx.doi.org/10.1016/j.gca.2016.06.002.

Peretyazhko, T. S., Ming, D. W., Rampe, E. B., Morris, R. V., and Agresti, D. G. (2018). Effect of solution pH and chloride concentration on akaganeite precipitation: Implications for akaganeite formation on Mars. *Journal of Geophysical Research: Planets*, *123*, 2211-2222, http://dx.doi.org/10.1029/2018JE005630.

Peretyazhko, T. S., Pan, M. J., Ming, D. W., Rampe, E. B., Morris, R. V., and Agresti, D. G. (2019). Reaction of akaganeite with Mars-relevant anions. *ACS Earth and Space Chemistry*, *3*(2), 314-323, http://dx.doi.org/10.1021/acsearthspacechem.8b00173.

Rapin, W., Meslin, P.-Y., Maurice, S., Vaniman, D., Nachon, M., Schroder, S., Gasnault, O., Forni, O., Wiens, R. C., Martínez, G. M., Cousin, A., Sautter, V., Lasue, J., Rampe, E. B., and Archer, D. (2016). Hydration state of calcium sulfates in Gale crater, Mars: Identification of bassanite veins. *Earth and Planetary Science Letters*, *452*, 197-205, http://dx.doi.org/10.1016/j.epsl.2016.07.045.

Refait, P., and Génin, J. -M. R. (1997). The mechanisms of oxidation of ferrous hydroxychloride β-$Fe_2(OH)_3Cl$ in aqueous solution: The formation of akaganeite vs. goethite. *Corrosion Science*, *39*(3), 539-553, http://dx.doi.org/10.1016/S0010-938X(97)86012-1.

Rémazeilles, C., and Refait, P. (2007). On the formation of β-FeOOH (akaganeite) in chloride-containing environments. *Corrosion Science*, *49*(2), 844-857, http://dx.doi.org/10.1016/j.corsci.2006.06.003.

Rice, M. S., Gupta, S., Treiman, A. H., Stack, K. M., Calef, F., Edgar, L. A., Grotzinger, J., Lanza, N., Le Deit, L., Lasue, J., Siebach, K. L., Vasavada, A., Wiens, R. C., Williams, J. (2017). Geologic overview of the Mars Science Laboratory rover mission at the Kimberley, Gale crater, Mars. *J. Geophysical Research: Planets*, *122*(1), 2-20, http://dx.doi.org/10.1002/2016JE005200.

Riech, V., and von Rad, U. (1979). Silica diagenesis in the Atlantic Ocean: diagenetic potential and transformations. In: Talwani, M., Hay, W., and Ryan, W. B. F. (eds.). Deep drilling results in the Atlantic Ocean: continental margins and paleoenvironment. M. Ewing series 3, *American Geophysical Union*, Washington D.C., pp. 315-340.

Schwertmann, U., and Cornell, R. M. (2000). Iron oxides in the laboratory: preparation and characterization. John Wiley & Sons.

Schwertmann, U., and Latham, M. (1986). Properties of iron oxides in some New Caledonian oxisols. *Geoderma*, *39*(2), 105-123.

Schwertmann, U., Friedl, J., Stanjek, H., Schulze, D. G. (2000). The effect of Al on Fe oxides. XIX. Formation of Al-substituted hematite from ferrihydrite at 25°C and pH 4 to 7. *Clays and Clay Minerals*, *48*(2), 159-172, http://dx.doi.org/10.1180/000985500547034.

Seeger, C. M., Marikos, M. A., and Nuelle, L. M. (1989) The Pilot Knobb hematite deposit. In: Brown, V. M., Kisvarsanyi, E., and Hagni, R. (Eds.), "Olympic Dam-type" Deposits and Geology of Middle Proterozoic Rocks in the St. Francois Mountains Terrane, Missouri: Guidebook, Vol. 4. Dociety of economic Geologists, Fort Collins, pp. 55-68.

Sherman, G. D., Ikawa, H., Uehara, G., and Okazaki, E. (1962). Types of occurrence of nontronite and nontronite-like minerals in soils. *Pacific Science*, *16*, 57-62.

Siebach, K. L., Baker, M. B., Grotzinger, J. P., McLennan, S. M., Gellert, R., Thompson, L. M., Hurowitz, J. A. (2017). Sorting out compositional trends in sedimentary rocks of the Bradbury

group (Aeolis Palus), Gale crater, Mars. *Journal of Geophysical Research – Planets*, *122*(2), 295-328.

Sleep, N. H. (1991). Hydrothermal circulation, anhydrite precipitation, and thermal structure at ridge axes. *Journal of Geophysical Research - Solid Earth*, *96*(B2), 2375-2387, http://dx.doi.org/10.1029/90JB02335.

Smith, D. K. (1998). Opal, cristobalite, and tridymite: Noncrystallinity versus crystallinity, nomenclature of the silica minerals and bibliography. *Powder Diffraction*, *13*(1), 2-19, http://dx.doi.org/10.1017/S0885715600009696.

Smith, R. J., Rampe, E. B., Horgan, B. H. N., and Dehouck, E. (2018). Deriving amorphous component abundance and composition of rocks and sediments on Earth and Mars. *Journal of Geophysical Research: Planets*, *123*(10), 2485-2505, http://dx.doi.org/10.1029/2018JE005612.

Stack, K.M., Grotzinger, J.P., Lamb, M.P., Gupta, S., Rubin, D.M., Kah, L.C., Edgar, L.A., Fey, D.M., Hurowitz, J.A., McBride, M., Rivera-Hernández, F., Sumner, D.Y., Van Beek, J.K., Williams, R.M.E., Yingst, R.A., 2018. Evidence for plunging river plume deposits in the Pahrump Hills member of the Murray formation, Gale crater, Mars. *Sedimentology*, *66*(5), 1768-1802, http://dx.doi.org/ 10.1111/sed.12558.

Ståhl, K., Nielsen, K., Jiang, J., Lebech, B., Hanson, J. C., Norby, P., van Lanschot, J. (2003). On the akaganeite crystal structure, phase transformations and possible role in post-excavational corrosion of iron artifacts. *Corrosion Science*, *45*, 2563-2575, http://dx.doi.org/10.1016/S0010-938X(03)00078-7.

Stanjek, H., Schwertmann, U. (1992). The influence of aluminum on iron oxidews. Part XVI: Hydroxyl and aluminum substitution in synthetic hematites. *Clays and Clay Minerals*, *40*(3), 347-354, http://dx.doi.org/10.1346/CCMN.1992.0400316.

Sun, S., Konhauser, K. O., Kappler, A., Li, Y.-L. (2015). Primary hematite in Neoarchean to Paleoproterozoic oceans. *GSA Bulletin*, *127*(5-6), 850-861, http://dx.doi,org/10.1130/B31122.1.

Taylor, S. R., McLennan, S. M. (2009). Planetary Crusts: Their Composition, Origin and Evolution, 378 pp., Cambridge University Press, Cambridge, U. K.

Thompson, L. M., Berger, J. A., Spray, J. G., Fraeman, A. A., McCraig, M. A., O'Connell-Cooper, C., Schmidt, M. E., VanBommel, S., Gellert, R., Yen, A., Boyd, N. I. (this issue). APXS-derived compositional characteristics of the Vera Rubin ridge, Gale crater, Mars: Geochemical implications for the origin of the ridge. *Journal of Geophysical Research: Planets*.

Tosca, N. J., Knoll, A. H. (2009). Juvenile chemical sediments and the long term persistence of water at the surface of Mars. *Earth and Planetary Science Letters*, *286*, 379-386, http://dx.doi.org/10.1016/j.epsl.2009.07.004.

Torrent, J., Guzman, R., and Parra, M. A. (1982). Influence of relative humidity on the crystallization of Fe(III) oxides from ferrihydrite. *Clays and Clay Minerals*, *30*(5), 337-340, http://dx.doi.org/10.1346/CCMN.1982.

Treiman, A. H., Morris, R. V., Agresti, D. G., Graff, T. G., Achilles, C. N., Rampe, E. B., Bristow, T. F., Ming, D. W., Blake, D. F., Vaniman, D. T., Bish, D. L., Chipera, S. J., Morrison, S. M., and Downs, R. T. (2014). Ferrian saponite from the Santa Monica Mountains (California, USA, Earth): Characterization as an analog for clay minerals on Mars with application to Yellowknife Bay in Gale Crater. *American Mineralogist*, *99*(11-12), 2234-2250, http://dx.doi.org/10.2138/am-2014-4763.

Turner, S. M. R., Schwenzer, S. P., Bridges, J. C., Rampe, E. B., Bedford, C. C., Achilles, C. N., McAdam, A. C., Mangold, N., Hicks, J., Parnell, J., and Kirnbauer, T. (this issue). Fluid-rock reactions in the Murray formation and Vera Rubin ridge, Gale crater, Mars. *Journal of Geophysical Research: Planets*.

Van Driessche, A. E. S., Stawski, T. M., Benning, L. G., and Kellermeier, M. (2017). Calcium sulfate precipitation throughout its phase diagram. In New Perspectives on Mineral Nucleation and Growth, chapter 12, p. 227–256. *Springer*, http://dx.doi.org/10.1007/978-3-319-45669-0_12.

VanBommel, S. J., Gellert, R., Berger, J. A., Campbell, J. L., Thompson, L. M., Edgett, K. S., McBride, M. J., Minitti, M. E., Pradler, I., and Boyd, N. I. (2016). Deconvolution of distinct lithology chemistry through oversampling with Mars Science Laboratory Alpha Particle X-ray Spectrometer. *X-ray Spectrometry*, *45*(3), 155-161, http://dx.doi.org/10.1002/xrs.2681.

VanBommel, S. J., Gellert, R., Berger, J. A., Thompson, L. M., Edgett, K. S., McBride, M. J., Minitti, M. E., Boyd, N. I., and Campbell, J. L. (2017). Modeling and mitigation of sample relief effects applied to chemistry measurements by the Mars Science Laboratory Alpha Particle X-ray Spectrometer. *X-ray Spectrometry*, *46*(4), 229-236, http://dx.doi.org/10.1002/xrs.2755.

Van Breemen, N. (1982). Genesis, morphology, and classification of acid sulfate soils in coastal plains. In: Kittrick, J. A., Fanning, D. S., and Hossner, L. R. (Eds.), Soil Science Society of America, pp. 95-108. Madison, Wisconsin U.S.A.

Vaniman, D. T., Bish, D. L., Chipera, S. J., Fialips, C. I., Carey, J. W., and Feldman, W. C. (2004). Magnesium sulphate salts and the history of water on Mars. *Nature*, *431*, 663-665, http://dx.doi.org/10.1038/nature02973.

Vaniman, D. T., Bish, D. L., Ming, D. W., Bristow, T. F., Morris, R. V., Blake, D. F., Chipera, S. J., Treiman, A. H., Rampe, E. B., Rice, M., Achilles, C. N., Grotzinger, J. P., McLennan, S. M., Williams, J., Bell III, J. F., Newsom, H. E., Downs, R. T., Maurice, S., Sarrazin, P., Yen, A. S., Morookian, J. M., Farmer, J. D., Stack, K., Milliken, R. E., Ehlmann, B. L., Sumner, D. Y., Berger, G., Crisp, J. A., Hurowitz, J. A., Anderson, R., Des Marais, D. J., Stolper, E. M., Edgett, K. S., Gupta, S., Spanovich, N., MSL Science Team, (2014). Mineralogy of a mudstone at Yellowknife Bay, Gale crater, Mars. *Science*, *343*(6169), 1243480.

Vaniman, D. T., Martínez, G. M., Rampe, E. B., Bristow, T. F., Blake, D. F., Yen, A. S., Ming, D. W., Rapin, W., Meslin, P. -Y., Morookian, J. M., Downs, R. T., Chipera, S. J., Morris, R. V., Morrison, S. M., Treiman, A. H., Achilles, C. N., Robertson, K., Grotzinger, J. P., Hazen, R. M., Wiens, R. C., and Sumner, D. Y. (2018). Gypsum, bassanite, and anhydrite at Gale crater, Mars. *American Mineralogist*, *103*(7), 1011-1020, http://dx.doi.org/10.2138/am-2018-6346.

Vaucher, J., Baratoux, D., Mangold, N., Pinet, P., Kurita, K., Grégoire, M. (2009). The volcanic history of central Elysium Planitia: Implications for martian magmatism. *Icarus*, *204*(2), 418-442.

Weibel, R., and Grobety, B. (1999). Pseudomorphous transformation of goethite needles into hematite in sediments of the Triassic Skagerrak Formation, Denmark. *Clays and Clay Minerals*, *34*(4), 657-660, http://dx.doi.org/10.1180/000985599543415.

Williams, R. M. E., Grotzinger, J. P., Dietrich, W. E., Gupta, S., Sumner, D. Y., Wiens, R. C., Mangold, N., Malin, M.C., Edgett, K. S., Maurice, S., Forni, O., Gasnault, O., Ollila, A., Newsom, H. E., Dromart, G., Palucis, M. C., Yingst, R. A., Anderson, R. B., Herkenhoff, K. E., Le Mouelic, S., Goetz, W., Madsen, M. B., Koefoed, A., Jensen, J. K., Bridges, J. C., Schwenzer, S. P., Lewis, K. W., Stack, K. M., Rubin, D., Kah, L. C., Bell III, J. F., Farmer, J. D., Sullivan, R., Van Beek, J., Blaney, D. L., Pariser, O., Deen, R. G., and the MSL Science Team (2013). Martian fluvial conglomerates at Gale crater. *Science*, *340*(6136), 1068-1072, http://dx.doi.org/10.1126/science.1237317.

Yen, A. S., Ming, D. W., Vaniman, D. T., Gellert, R., Blake, D. F., Morris, R. V., Morrison, S. M., Bristow, T. F., Chipera, S. J., Edgett, K. S., Treiman, A. H., Clark, B. C., Downs, R. T., Farmer, J. D., Grotzinger, J. P., Rampe, E. B., Schmidt, M. E., Sutter, B., Thompson, L. M., and the MSL Science Team (2017). Multiple stages of aqueous alteration along fractures in mudstone and sandstone strata in Gale Crater, Mars. *Earth and Planetary Science Letters*, *471*, 186-198, http://dx.doi.org/10.1016/j.epsl.2017.04.033.

Zhao, J., Lin, W., Chang, Q., Li, W., and Lai, Y. (2012). Adsorptive characteristics of akaganeite and its environmental applications: a review. *Environmental Technology Reviews*, *1*(1), 114-126, http://dx.doi.org/10.1080.09593330.2012.701239.

## Tables

Table 1. Mineral and X-ray amorphous abundances for Duluth, Stoer, Highfield, and Rock Hall. 1-sigma errors are reported in parentheses, where the error is applied to the last decimal place(s). Mineral abundances in the "xtal" columns are renormalized without phyllosilicate and amorphous abundances.

| | Duluth | | Stoer | | Highfield | | Rock Hall | |
|---|---|---|---|---|---|---|---|---|
| Phase | xtal | Bulk | xtal | bulk | xtal | bulk | Xtal | Bulk |
| Plagioclase | 56.4(12) | 27.1(6) | 44.5(20) | 23.2(10) | 47.3(21) | 19.9(9) | 38.2(41) | 20.2(22) |
| K-spar | 6.6(10) | 3.2(4) | 3.1(26) | 1.6(13) | 3.7(10) | 1.6(5) | -- | -- |
| Pyroxene | 9.5(25) | 4.5(11) | 6.4(16) | 3.3(9) | 10.1(34) | 4.2(15) | 17.1(19) | 9.1(10) |
| Hematite | 12.6(21) | 6.1(10) | 28.4(14) | 14.7(8) | 20.2(13) | 8.5(5) | 5.4(4) | 2.9(2) |
| Magnetite | 1.7(10) | 0.7(4) | 0.6(5) | 0.3(3) | 1.4(13) | 0.5(5) | -- | -- |
| Akaganeite | -- | -- | 2.4(13) | 1.2(7) | -- | -- | 11.3(9) | 6.0(5) |
| Jarosite | -- | -- | 2.0(5) | 1.0(3) | -- | -- | 4.3(9) | 2.3(5) |
| Anhydrite | 3.4(10) | 1.7(4) | 6.0(6) | 3.1(3) | 8.2(10) | 3.5(5) | 21.2(26) | 11.2(14) |
| Bassanite | 7.4(6) | 3.5(3) | 0.9(3) | 0.5(2) | 2.6(6) | 1.1(3) | -- | -- |
| Gypsum | 0.4(3) | 0.1(1) | 4.6(14) | 2.4(8) | 5.2(10) | 2.2(5) | -- | -- |
| Quartz | 2.1(8) | 1.0(4) | 1.2(7) | 0.7(4) | 1.3(7) | 0.5(3) | -- | -- |
| F-apatite[*] | -- | -- | -- | -- | -- | -- | 2.5(8) | 1.3(4) |
| Phyllosilicate | -- | 15(4) | -- | 10(3) | -- | 5(1) | -- | 13(3) |
| Opal-CT | -- | -- | -- | -- | -- | 4(1) | -- | -- |
| Amorphous | -- | 37[a] | -- | 38[a] | -- | 49[a] | -- | 34(8)[b] |

[*]Siderite provides a similar fit as fluorapatite to Rock Hall.

[a]Minimum amorphous abundance based on mass balance calculations

[b]Amorphous abundance based on FULLPAT analyses

Table 2. Refined unit-cell parameters in angstroms of the major phases in Duluth, Stoer, Highfield, and Rock Hall. 1-sigma errors are reported in parentheses, where the error is applied to the last decimal place(s).

| Mineral | Parameter | Duluth | Stoer | Highfield | Rock Hall |
|---|---|---|---|---|---|
| Plagioclase | a | 8.165(6) | 8.151(3) | 8.177(8) | 8.155(5) |
| | b | 12.864(6) | 12.865(9) | 12.879(12) | 12.875(1) |
| | c | 7.116(2) | 7.104(5) | 7.106(3) | 7.113(2) |
| | $\alpha$ | 93.46(4) | 93.32(4) | 92.86(30) | 93.43(5) |
| | $\beta$ | 116.27(2) | 116.23(2) | 116.33(4) | 116.25(2) |
| | $\gamma$ | 90.08(2) | 90.11(2) | 90.27(3) | 90.15(2) |
| Sanidine | a | | | 8.557(28) | |
| | b | | | 13.182(43) | |
| | c | | | 7.143(7) | |
| | $\beta$ | | | 116.67(19) | |
| Hematite | a | 5.039(8) | 5.028(2) | 5.042(3) | 5.039(3) |
| | c | 13.753(21) | 13.728(6) | 13.753(3) | 13.736(7) |
| Akaganeite | a | | | | 10.566(10) |
| | b | | | | 3.026(6) |
| | c | | | | 10.457(8) |
| | $\beta$ | | | | 89.66(14) |
| Anhydrite | a | 7.023(24) | 6.987(11) | 7.005(10) | 7.002(3) |
| | b | 7.036(36) | 7.004(18) | 6.995(14) | 6.991(3) |
| | c | 6.195(34) | 6.184(9) | 6.231(15) | 6.239(2) |
| Bassanite | a | 12.069(31) | | | |
| | b | 6.935(26) | | | |
| | c | 12.564(90) | | | |
| | $\beta$ | 31.13(28) | | | |

Table 3. Crystal chemistry of plagioclase in Duluth, Stoer, Highfield, and Rock Hall.

| Mineral | Duluth | Stoer | Highfield | Rock Hall |
|---|---|---|---|---|
| Plagioclase | $An_{34(4)}Ab_{64(4)}$ | $An_{41(4)}Ab_{59(4)}$ | $An_{28(3)}Ab_{72(3)}$ | $An_{44(7)}Ab_{56(6)}$ |

Table 4. Calculated composition of X-ray amorphous component in Duluth, Stoer, Highfield, and Rock Hall in wt.% oxides. Values in the "renorm" columns have been renormalized to 100%.

| | DU | DU renorm | ST | ST renorm | HF | HF renorm | RH | RH renorm |
|---|---|---|---|---|---|---|---|---|
| $SiO_2$ | 13.22 | 35.60 | 21.97 | 57.45 | 31.94 | 65.49 | 12.65 | 37.21 |
| $TiO_2$ | 1.06 | 2.87 | 1.04 | 2.71 | 0.88 | 1.80 | 1.00 | 2.95 |
| $Al_2O_3$ | 0.00 | 0.00 | 2.18 | 5.71 | 3.57 | 7.32 | 2.42 | 7.10 |
| $Cr_2O_3$ | 0.32 | 0.87 | 0.34 | 0.89 | 0.28 | 0.57 | 0.31 | 0.91 |
| $FeO_T$ | 7.99 | 21.52 | 0.00 | 0.00 | 3.63 | 7.44 | 4.09 | 12.03 |
| MnO | 0.21 | 0.57 | 0.17 | 0.45 | 0.15 | 0.31 | 0.08 | 0.24 |
| MgO | 2.06 | 5.54 | 4.21 | 11.00 | 3.59 | 7.36 | 1.86 | 5.48 |
| CaO | 2.75 | 7.41 | 1.59 | 4.15 | 0.01 | 0.03 | 1.71 | 5.02 |
| $Na_2O$ | 0.16 | 0.42 | 0.90 | 2.35 | 1.04 | 2.13 | 0.41 | 1.21 |
| $K_2O$ | 0.56 | 1.50 | 0.62 | 1.62 | 0.66 | 1.36 | 0.40 | 1.19 |
| $P_2O_5$ | 1.13 | 3.03 | 0.84 | 2.21 | 0.79 | 1.62 | 0.08 | 0.25 |
| $SO_3$ | 6.77 | 18.23 | 3.72 | 9.72 | 1.31 | 2.69 | 7.97 | 23.43 |
| Cl | 0.90 | 2.43 | 0.67 | 1.75 | 0.92 | 1.89 | 1.01 | 2.98 |
| Total | 37.14[a] | 99.99 | 38.25[a] | 100.01 | 48.77[a] | 100.01 | 33.99[b] | 100.00 |

[a]Minimum amorphous abundance based on mass balance calculations

[b]Amorphous abundance based on FULLPAT analyses

Table 5. FWHM of the hematite (104) peaks in Duluth, Stoer, Highfield, and Rock Hall. 1-sigma errors are reported in parentheses, where the error is applied to the last decimal place(s).

| Sample | Hematite (104) FWHM |
|---|---|
| Duluth | 0.66(18) |
| Stoer | 0.33(1) |
| Highfield | 0.38(1) |
| Rock Hall | 0.30(9) |

## Figures

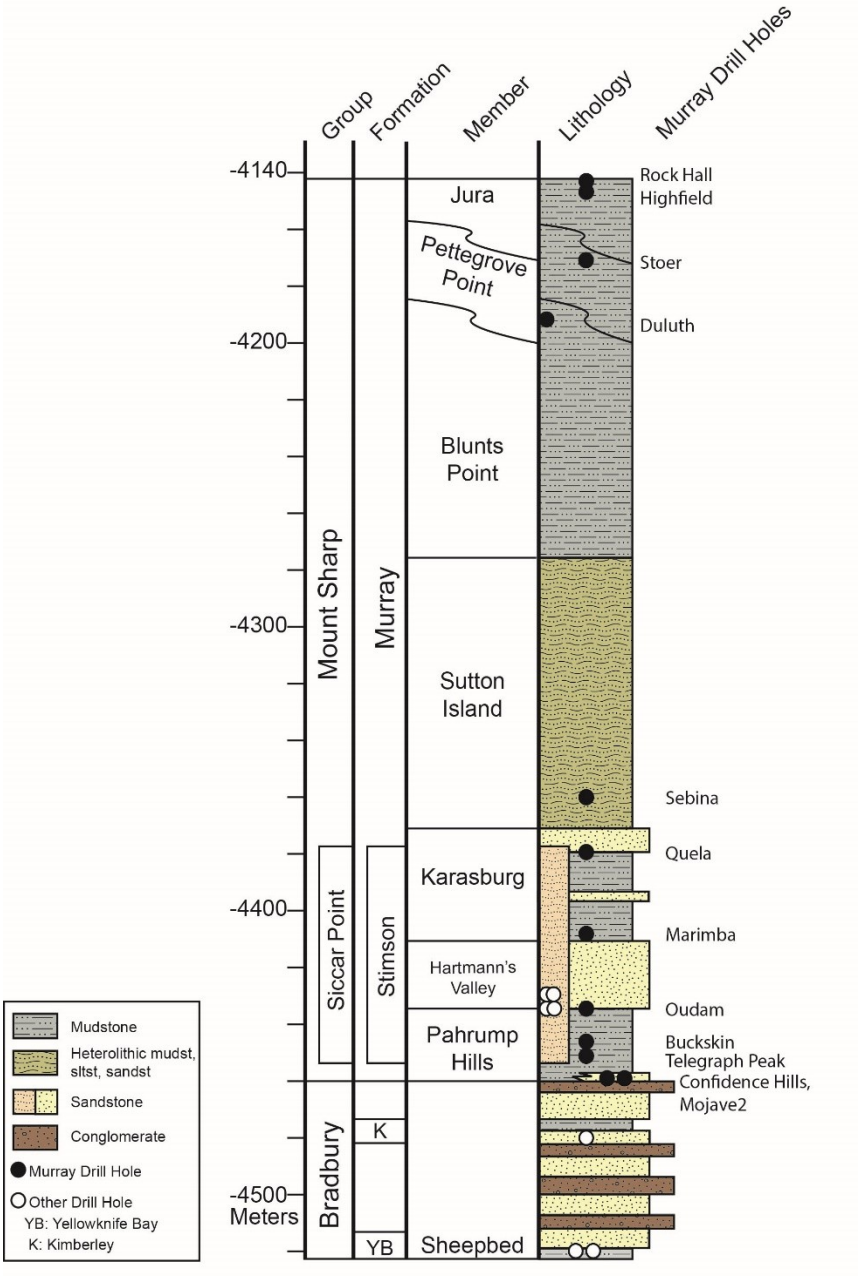


Figure 1. Stratigraphic column of units investigated by Curiosity from landing through the Vera Rubin ridge campaign. Figure credit: the MSL sedimentology and stratigraphy working group.

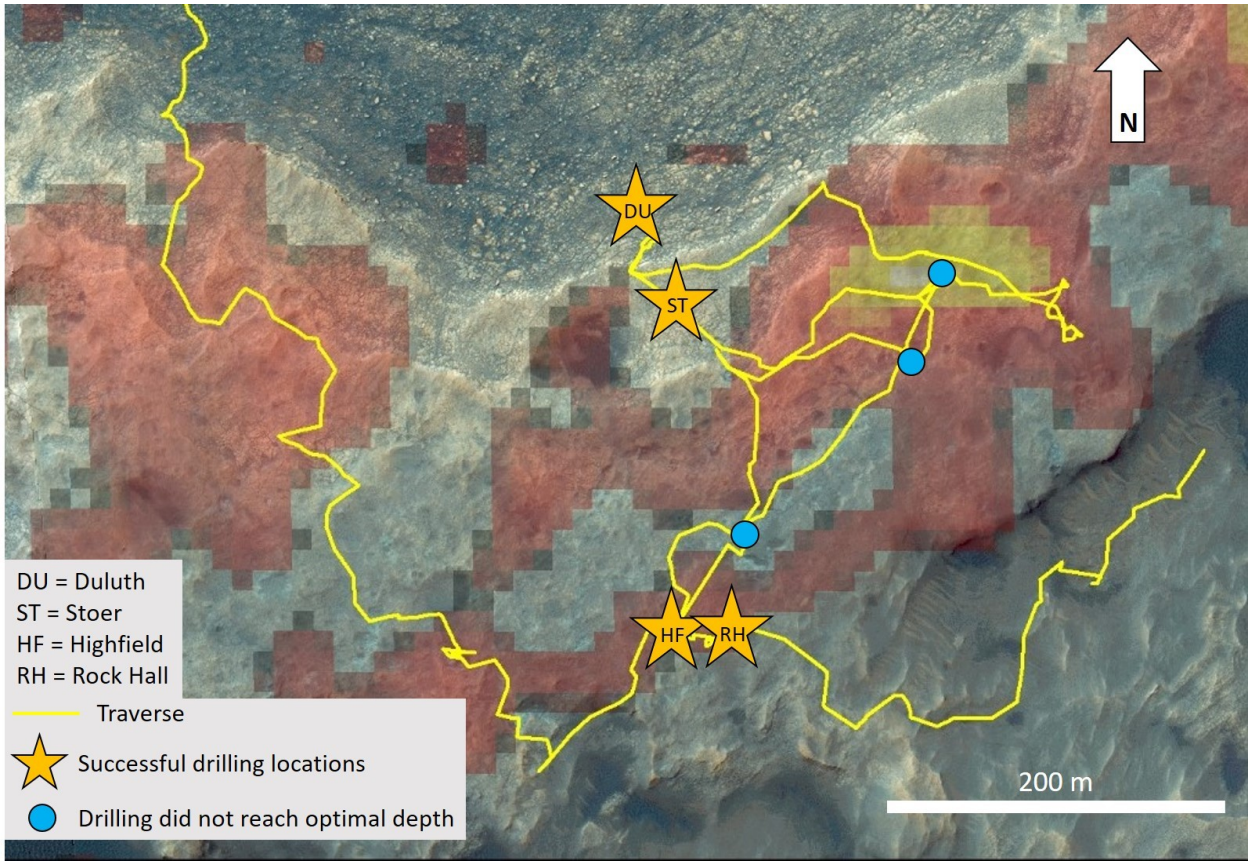


Figure 2. Map of Vera Rubin ridge drilling locations. Yellow line represents Curiosity's traverse. Stars denote successful drill sample locations and blue circles denote locations where drilling did not reach the full depth. Red and yellow pixels represent areas of strong and moderate hematite spectral signatures, respectively, from CRISM mapping (Fraeman et al., 2013; 2016).

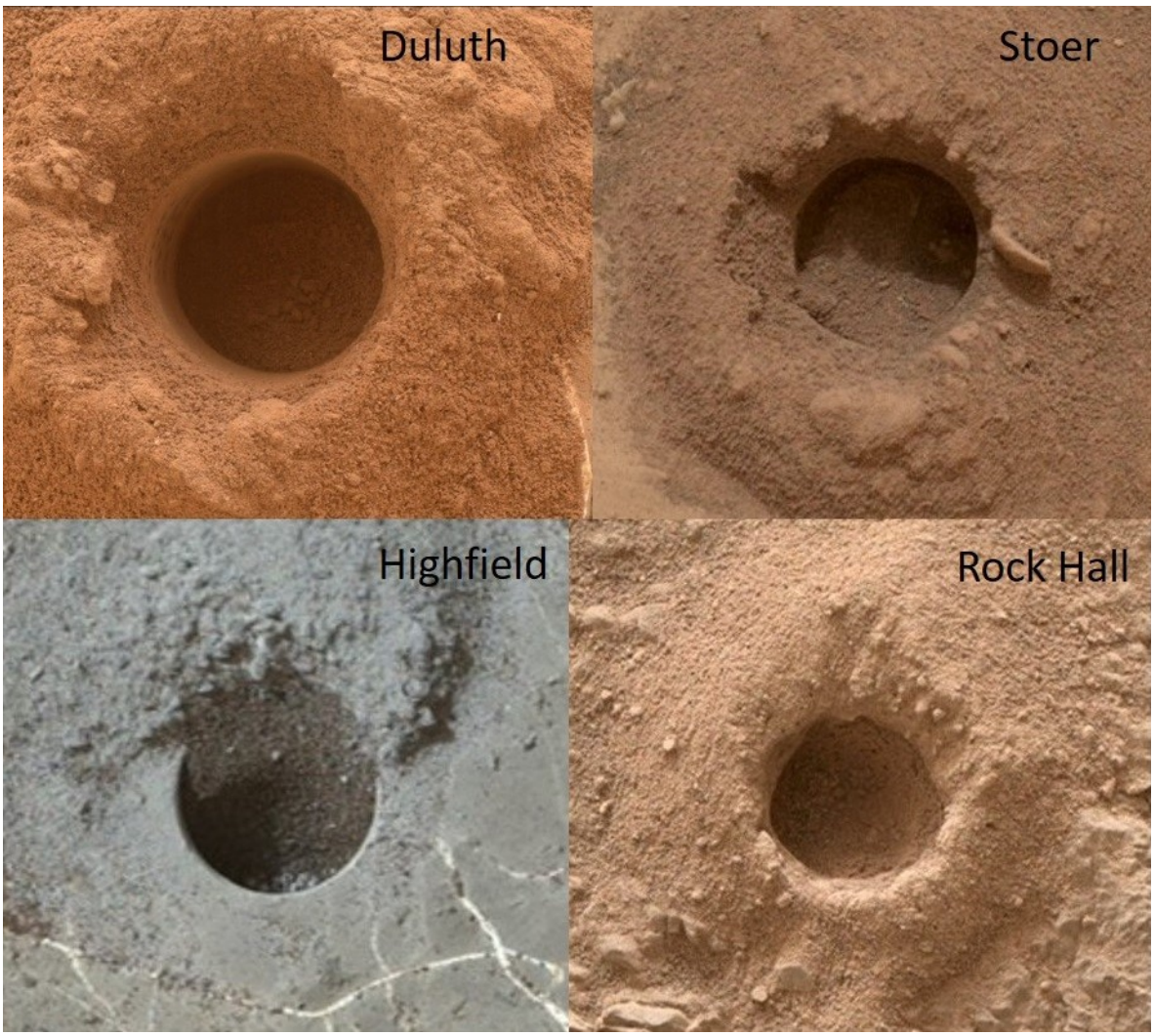


Figure 3. MAHLI images of successful drill holes. The diameter of each hole is ~1.3 cm.

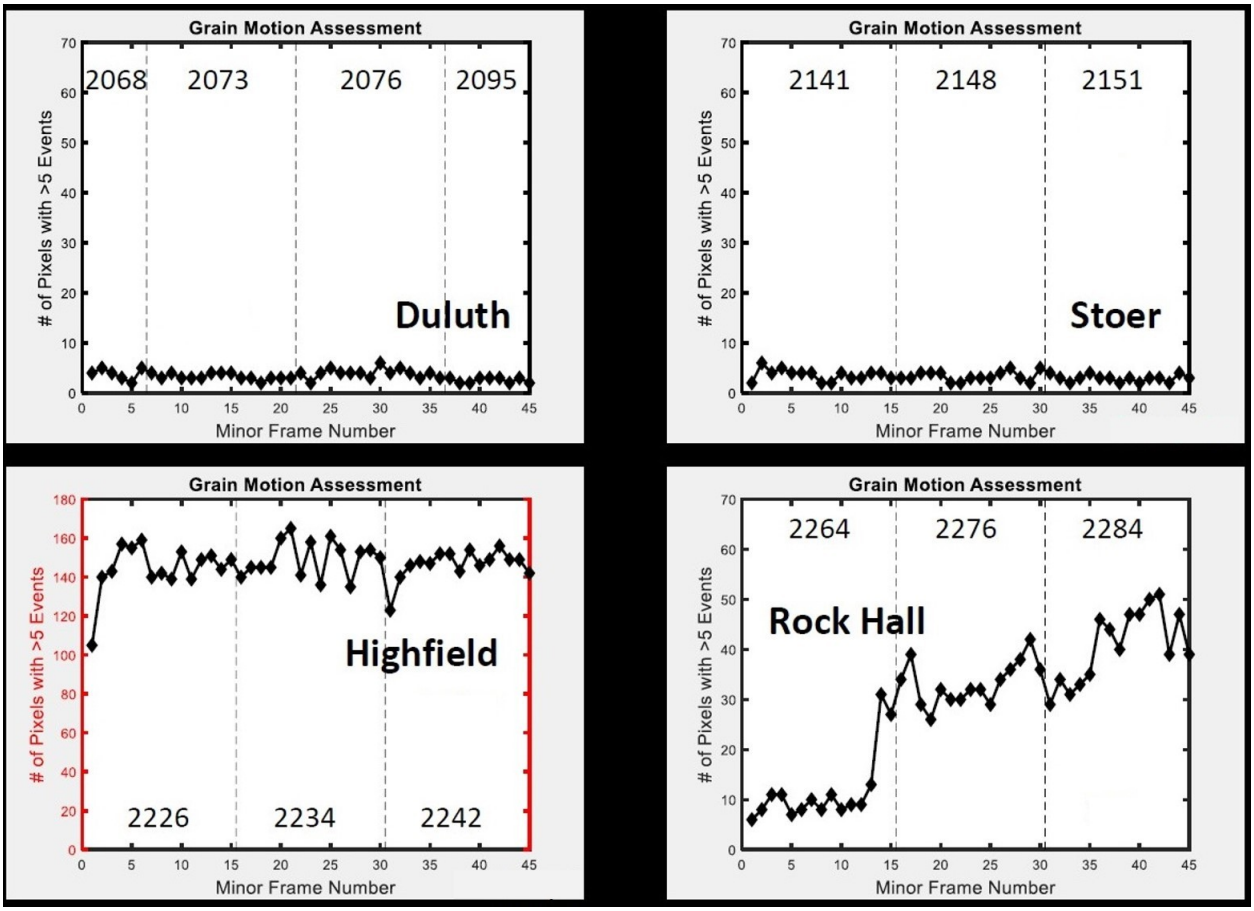


Figure 4. Grain motion assessments for the samples Duluth, Stoer, Highfield, and Rock Hall. When grain motion during an analysis is off-nominal, the number of photons that hit each pixel (i.e., the number of pixels with >5 photon events) increases. Vertical dashed lines designate different sols of analysis, and the sol numbers are listed at the top of each graph. Note the different y-axis for Highfield.

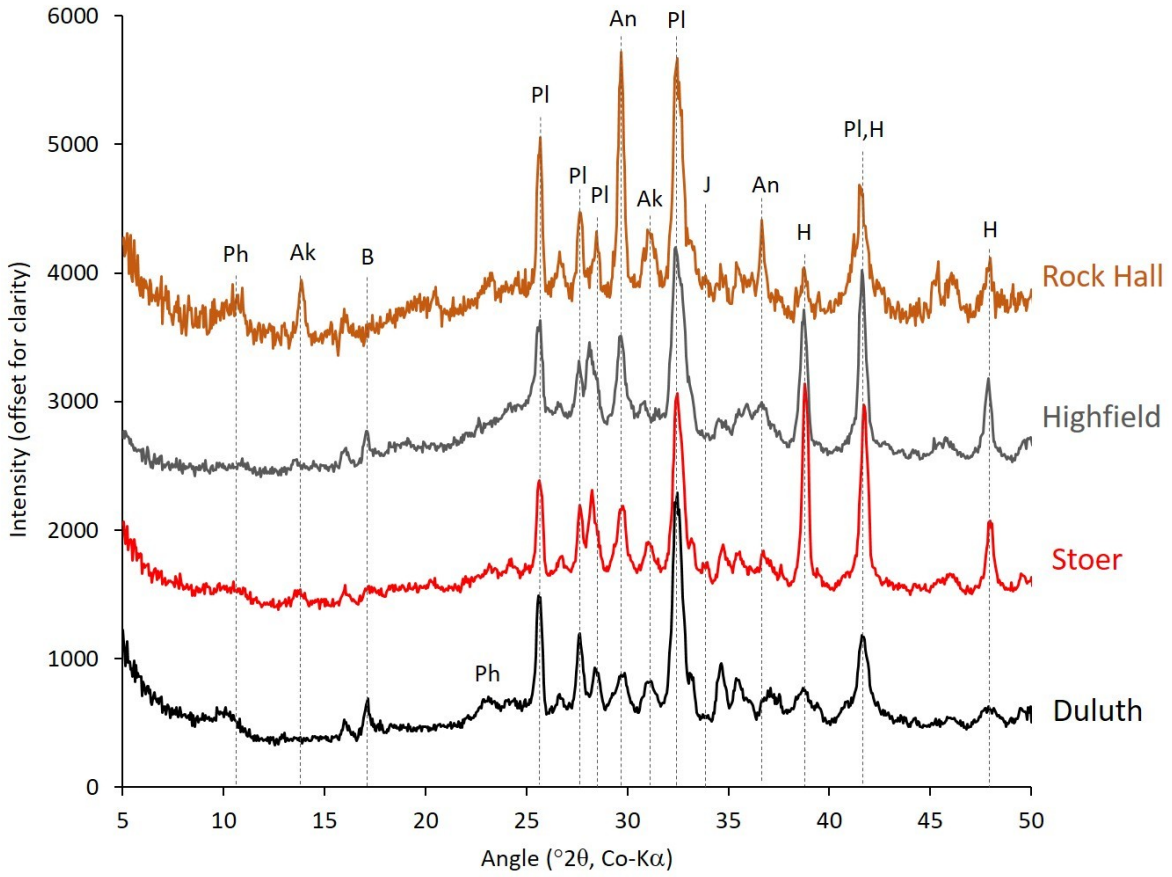


Figure 5. CheMin XRD patterns of the four drill samples collected from on and near Vera Rubin ridge. Major peaks are labeled. Ak = akaganeite, An = anhydrite, B = bassanite, H = hematite, J = jarosite, Ph = phyllosilicate, and Pl = plagioclase. The Rock Hall pattern consists of the first four minor frames and has been scaled to a total of 45 minor frames. Patterns are offset for clarity.

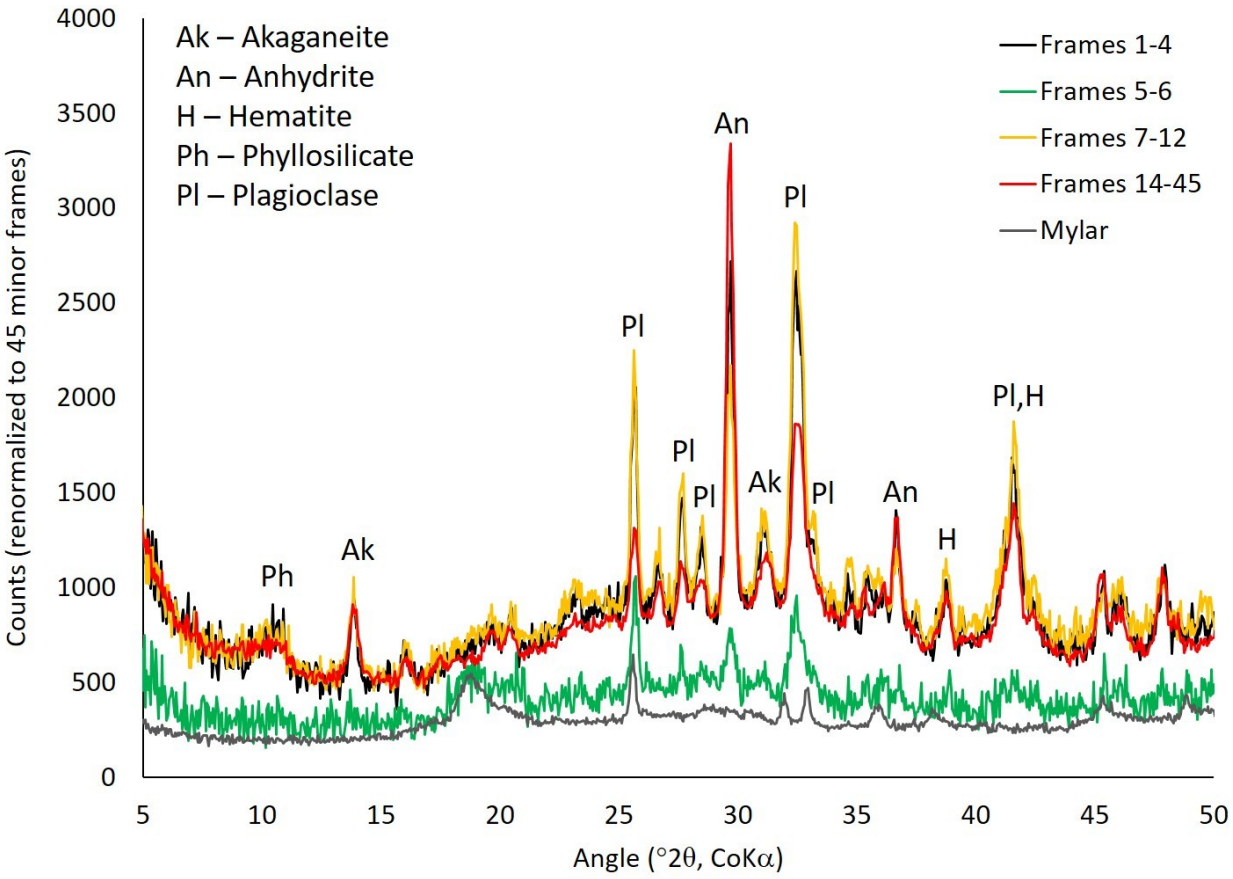


Figure 6. CheMin 1D diffraction patterns from different minor frames of the Rock Hall analysis. Peak heights from anhydrite (An) and plagioclase (Pl) vary significantly between frames 1-4, 7-12, and 14-45. The pattern from frames 5-6 (green pattern) resembles that of the empty Mylar cell (gray pattern).

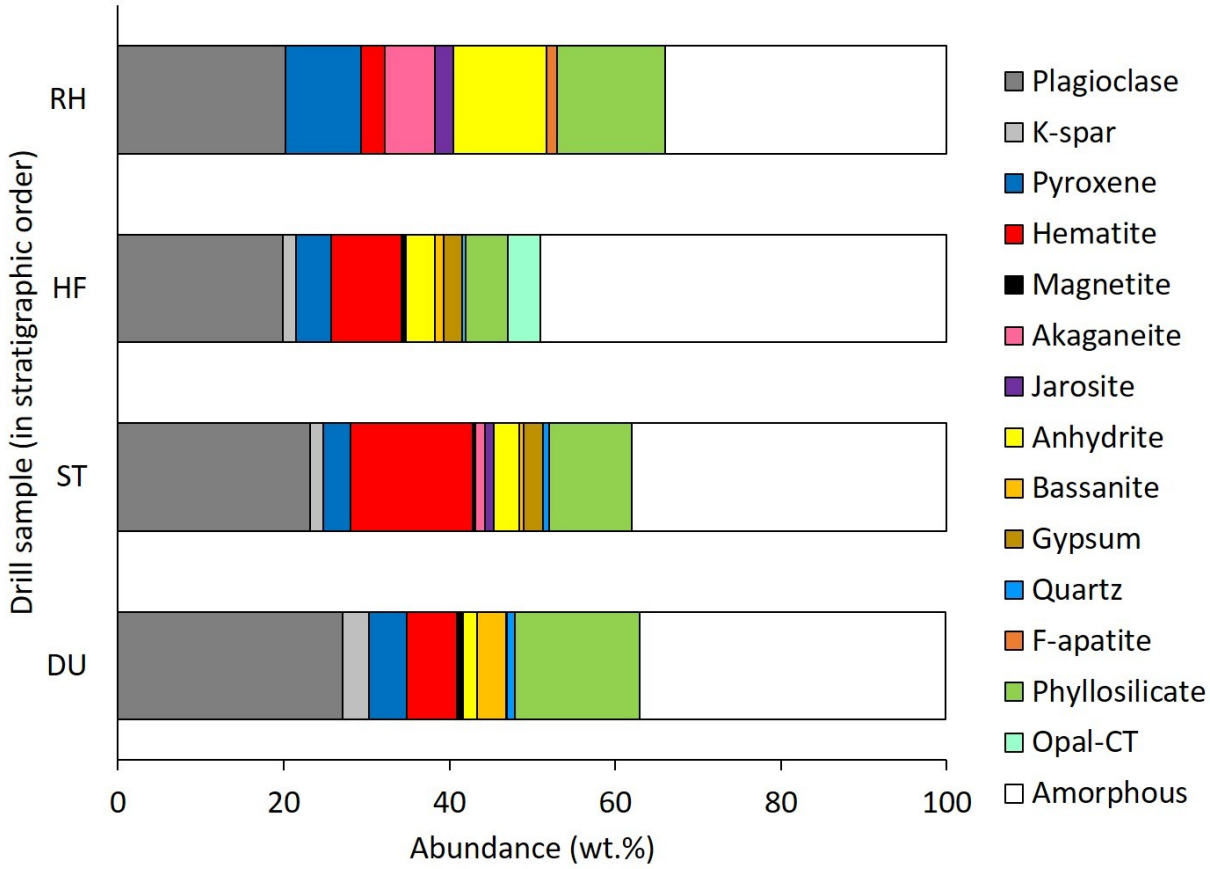


Figure 7. Bar graph showing the abundances of all crystalline phases and X-ray amorphous materials from all four drill samples collected on or near Vera Rubin ridge. DU = Duluth, ST = Stoer, HF = Highfield, and RH = Rock Hall.

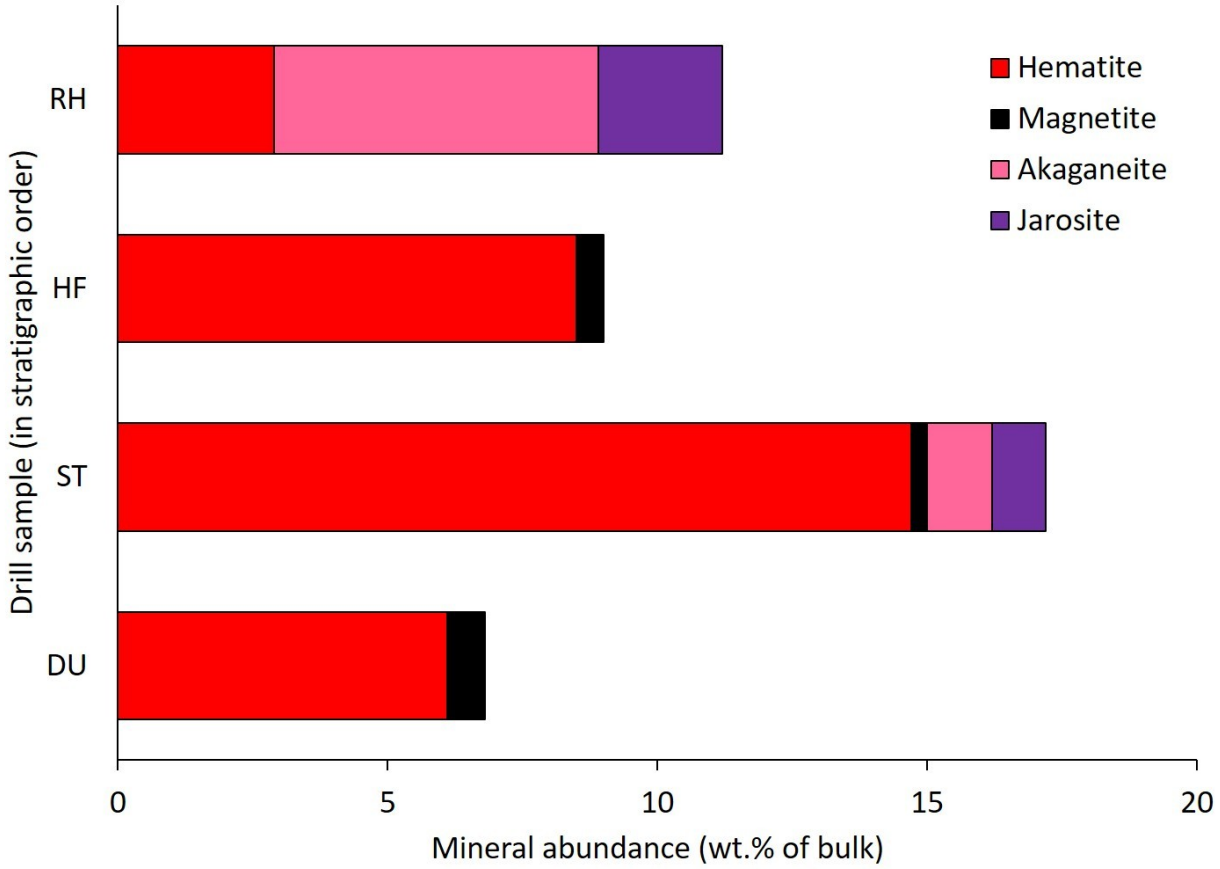


Figure 8. Bar graphs showing bulk mineral abundances of Fe-oxides, Fe-oxyhydroxides, and Fe-sulfates in the four drill samples collected from on and near Vera Rubin ridge. DU = Duluth, ST = Stoer, HF = Highfield, RH = Rock Hall.

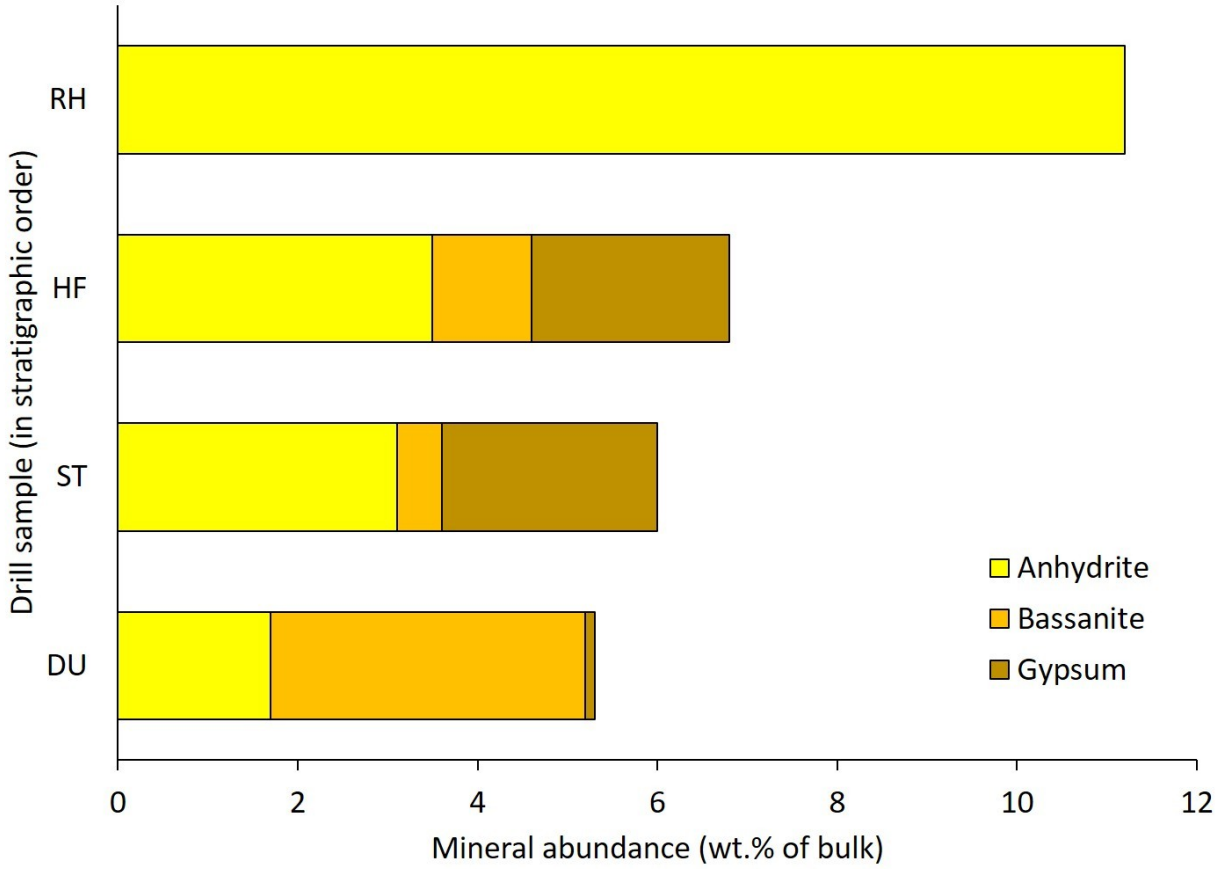


Figure 9. Bar graphs showing bulk mineral abundances of Ca-sulfates in the four drill samples collected from on and near Vera Rubin ridge. DU = Duluth, ST = Stoer, HF = Highfield, RH = Rock Hall.

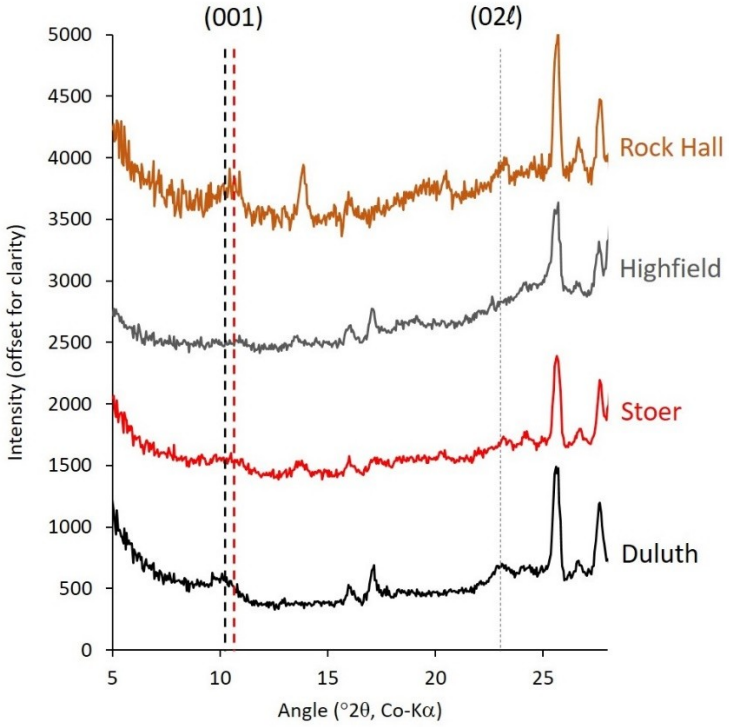


Figure 10. CheMin XRD patterns from 5-28 °2θ showing the position of the 001 and 02l phyllosilicate peaks. The bold dashed black line is at 10 Å, the bold dashed red line is at 9.6 Å, and the fine dashed black line is at 4.48 Å. The Rock Hall pattern consists of the first four minor frames and has been scaled to a total of 45 minor frames. Patterns are offset for clarity.

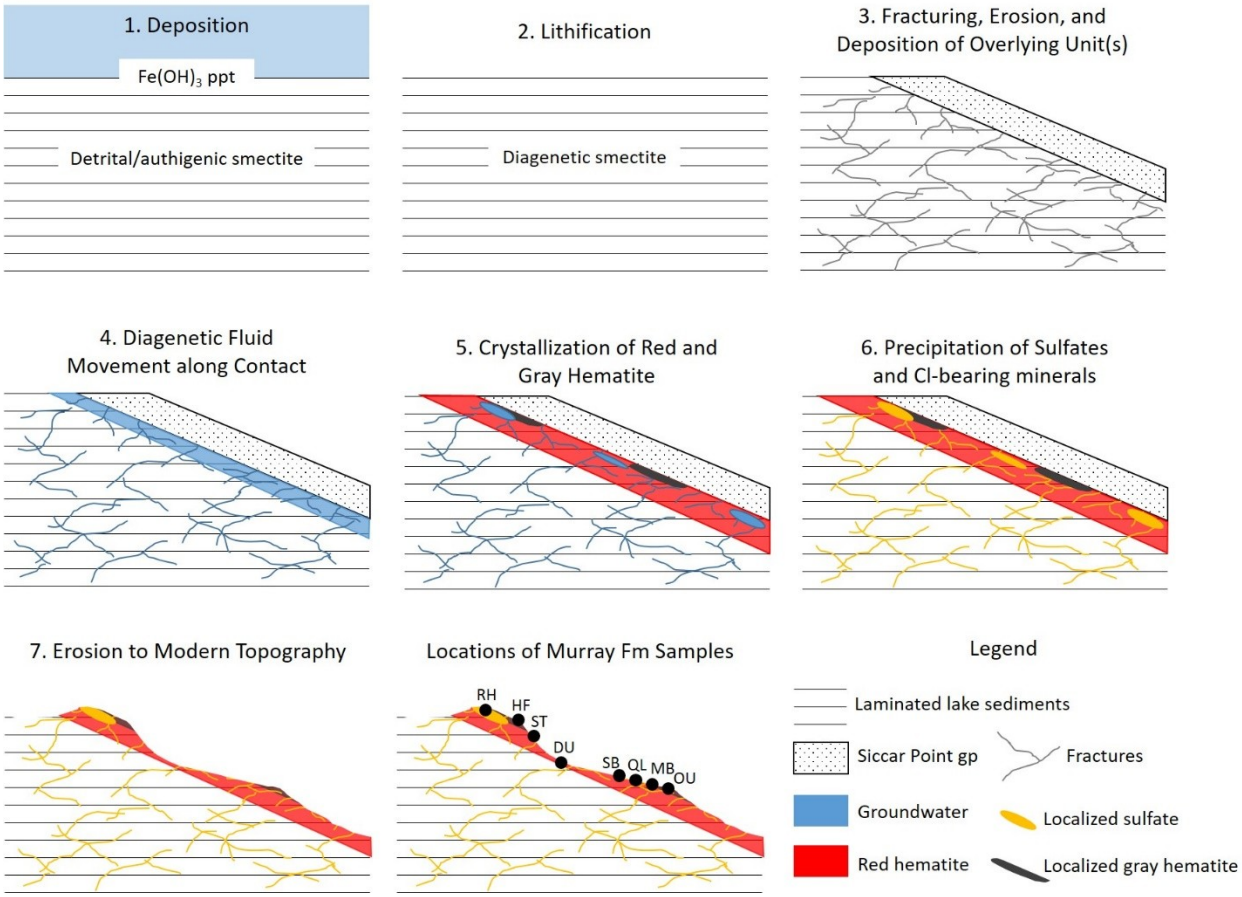


Figure 11. Conceptual model to explain the mineralogy of Vera Rubin ridge and the underlying Murray formation. (1) Layered fine-grained sediments are deposited in a lake, a ferrihydrite-like phase precipitates at the sediment-water interface, and smectite is a detrital component or forms as sediments are buried. (2) Lacustrine sediments are lithified. Smectite may form during early diagenesis if it is not detrital or formed syn-depositionally. (3) Lithified lacustrine mudstone fractures and is eroded, then the Siccar Point group is emplaced unconformably and becomes lithified. (4) Warm, acidic, and/or saline fluids permeate episodically along the contact between the Murray formation and Siccar Point group and within fractures. (5) Warm fluids cause the precipitation of gray hematite from ferrihydrite-like materials in select locations (shown as gray patches) and red hematite throughout much of the Murray formation (shown in red). As fluids cool and/or freeze, pockets of concentrated acid-saline fluids form. (6) Ca-sulfate, jarosite, and akaganeite form in the concentrated acid-saline pockets and Ca-sulfate precipitates in fractures (shown as yellow patches and fractures). Multiple late-stage fluid episodes could have precipitated Ca-sulfate in fractures and veins. (7) The Murray formation and Siccar Point group rocks are eroded to the modern topography, where VRR is resistant because of the precipitation of gray hematite and opaline silica from warm fluids. Warm fluids may have been concentrated in the contact just above VRR to allow for significant cementation of the sediments, but warm fluids also interacted with the Murray at the Oudam sample location. This model only shows the lake sediments in the Murray formation and the Siccar Point group sandstone for simplicity, but it is likely that the Murray formation was thicker or other units may have overlain it to allow for its lithification. Similarly, it is likely that other units were stratigraphically above the Siccar Point group to allow for its lithification. The depth of burial of these sediments is not well constrained,

and late diagenetic processes in steps 4-6 may not have occurred close to the surface as depicted here.

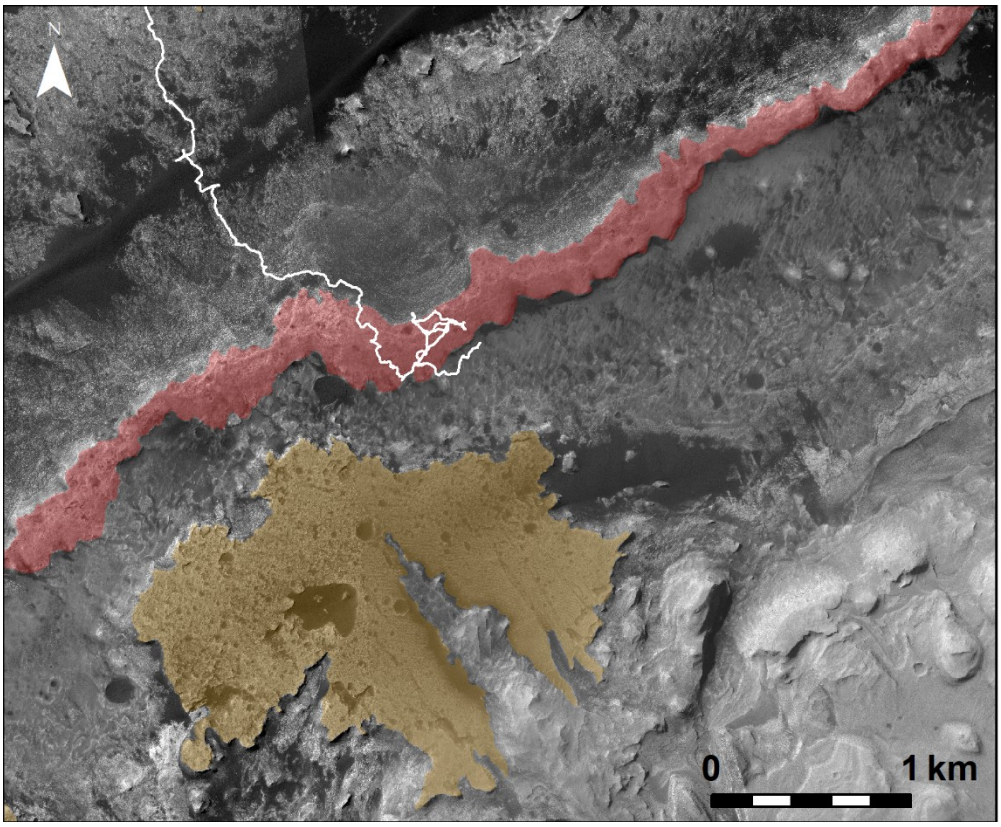


Figure 12. HiRISE mosaic showing the location of Vera Rubin ridge (highlighted in red) and its proximity to the Greenheugh capping unit (highlighted in brown). *Curiosity's* traverse through sol 2370 is shown in white.